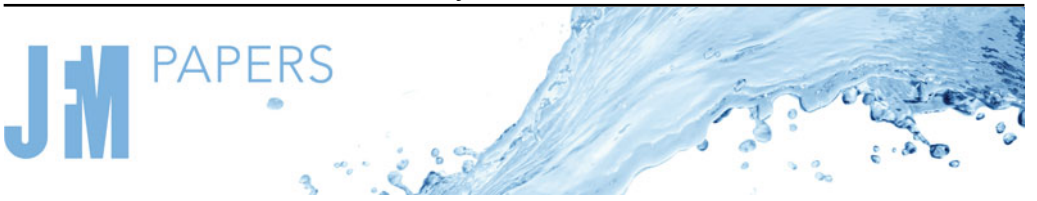
J. Fluid Mech. (2026), *vol.* 1042, A5, doi:10.1017/jfm.2026.11941



Vortex-induced vibration forever of an extreme-light cylinder in an unsteady wake

Shenfang Li[1], **Peng Han**[2], **Wei-Xi Huang**[3,4] **and Junlei Wang**[1]

[1]School of Mechanical and Power Engineering, Zhengzhou University, Zhengzhou 450000, PR China

[2]State Key Laboratory for Strength and Vibration of Mechanical Structures and School of Aerospace, Xi'an Jiaotong University, Xi'an 710049, PR China

[3]AML, Department of Engineering Mechanics, Tsinghua University, Beijing 100084, PR China

[4]State Key Laboratory of Advanced Space Propulsion, Tsinghua University, Beijing 100084, PR China

Corresponding authors: Peng Han, hanpeng@xjtu.edu.cn; Junlei Wang, jlwang@zzu.edu.cn

(Received 20 February 2026 UTC; revised 10 June 2026 UTC; accepted 15 July 2026 UTC)

Vortex-induced vibration forever (VIVF) is classically associated with a single elastically mounted cylinder, for which oscillations persist at infinite reduced velocity when the mass ratio (m^*) falls below a critical value (m^*_{cr}). The existence and characteristics of such permanent vibration under unsteady wake conditions remain unclear. This study investigates the vibration response of an extreme-light cylinder placed in the wake of an upstream fixed cylinder without restoring forces, with particular emphasis on the existence and variation of a critical mass ratio m^*_{cr} with the spacing ratio (L/D). The Reynolds number is set to 60, the mass ratio m^* ranges from 0.2 to 14 and the spacing ratio L/D ranges from 1.1 to 6.0. Three vibration regimes are identified in the (L/D, m^*) parameter space: non-vibration (NV), limited-range vibration (LRV) and infinite-range vibration (IRV). A critical mass ratio m^*_{cr} emerges at the LRV–NV boundary, where the vibration amplitude continuously diminishes to zero as m^* approaches m^*_{cr}, in contrast to the abrupt transition observed in single-cylinder VIVF; this extinction coincides with the disappearance of the second-order flow mode. Furthermore, m^*_{cr} is governed by the spacing ratio relative to the vortex formation length L_f/D of a stationary cylinder: when $L/D < L_f/D$, m^*_{cr} increases with L/D, whereas for $L/D > L_f/D$, it decreases with further increase in L/D. In contrast, within the IRV regime the flow maintains persistent co-shedding behaviour and no critical mass ratio is observed within the investigated m^* range, indicating that wake interference reshapes the stability boundary of the system.

Key words: flow-structure interactions, vortex shedding

https://doi.org/10.1017/jfm.2026.11941 Published online by Cambridge University Press

© The Author(s), 2026. Published by Cambridge University Press.

1. Introduction

The flow-induced vibration (FIV) of elastically mounted circular cylinders has attracted significant research interest in engineering applications, including offshore platform risers, bridge cables and other structural systems. The FIV research primarily focuses on complex vortex dynamics and fluid–structure interaction mechanisms, with the objectives of mitigating undesirable vibration energy or exploring potential energy-harvesting applications (Luo *et al.* 2022; Lo *et al.* 2024). The FIV phenomena can be classified according to distinct excitation mechanisms, including vortex-induced vibration (VIV), which arises from periodic vortex shedding (Williamson & Govardhan 2008; Konstantinidis *et al.* 2021), wake-induced vibration (WIV), which is triggered by unsteady wake interactions (Assi *et al.* 2010; Fan *et al.* 2021), as well as galloping and flutter, which are also typical FIV phenomena (Barrero-Gil *et al.* 2009; Han & de Langre 2021). Comprehensive reviews of FIV classifications and the underlying physical mechanisms can be found in the literature (Wang *et al.* 2020*a*; Huera-Huarte 2025).

The VIV and WIV of circular cylinders both involve intricate vortex dynamics. The VIV phenomena and their underlying mechanisms for single cylinders are first reviewed to provide essential insights for understanding WIV in tandem-cylinder systems. Despite the apparent simplicity of the structural configuration in VIV, the associated fluid dynamics exhibits remarkable complexity, which has sustained extensive research efforts (Williamson & Govardhan 2004; Zhao 2023). An important characteristic of VIV is the lock-in phenomenon, in which the vortex-shedding frequency synchronises with the structural vibration frequency and remains close to the natural frequency of the system (Gabbai & Benaroya 2005). The lock-in phenomenon typically occurs within a limited range of reduced velocity U_r. The lock-in of VIV can be divided into upper and lower branches at low mass–damping parameters $m^*\zeta$, whereas only the lower branch persists at high $m^*\zeta$ (Morse & Williamson 2009; Mishra *et al.* 2020; Han *et al.* 2026). Here, the mass ratio m^* represents the ratio of the structural mass to the displaced fluid mass, while ζ denotes the ratio of the structural damping to the critical damping. Beyond the lock-in regime, desynchronised branches emerge. The mass ratio m^* plays a critical role in VIV dynamics. When m^* of a circular cylinder falls below the critical mass ratio, the cylinder undergoes VIV forever; that is, the lock-in range becomes infinite. Experiments and numerical simulations have identified a critical mass ratio of $m^*_{cr} = 0.54$ (Govardhan & Williamson 2002; Han *et al.* 2023*b*), below which large-amplitude vibrations persist even at infinite reduced velocity. Notably, recent studies have confirmed that m^*_{cr} exhibits a dependence on the Reynolds number (Navrose & Mittal 2017; Bourguet 2023, 2024).

For fixed tandem cylinders, the flow field exhibits diverse characteristics under different spacing ratios and Reynolds numbers (Zdravkovich 1987; Alam *et al.* 2003; Sumner 2010). Compared with the VIV of a single circular cylinder, the WIV of tandem cylinders exhibits substantially greater complexity (Nguyen *et al.* 2018; Wang *et al.* 2018; Alam *et al.* 2023). In addition to the key parameters governing VIV, U_r, m^*, ζ and the Reynolds number, the spacing ratio L/D emerges as a critical parameter in WIV dynamics. Bokaian & Geoola (1984) identified four distinct WIV regimes through comprehensive experiments with $m^*\zeta = 0.109$: wake-induced galloping (WIG), VIV, separated VIV and WIG, and combined VIV and WIG. The VIV is observed at relatively low U_r, with vibration frequencies close to the natural frequency of the system, whereas WIG occurs at higher U_r with vibration frequencies exceeding the natural frequency. Similar vibration responses were reported by Hu *et al.* (2020), who demonstrated that $m^*\zeta$ significantly affects vibration amplitude, velocity range and hysteresis behaviour. Numerical simulations of fluid–structure interaction for tandem cylinders have been conducted by several researchers

https://doi.org/10.1017/jfm.2026.11941 Published online by Cambridge University Press

(Bao *et al.* 2012; Sharma & Bhardwaj 2023), focusing on vibration modes, lock-in mechanisms, gap flow dynamics, fluid forces and wake characteristics. Alam *et al.* (2025) showed that increasing L/D initially amplifies the influence of the upstream cylinder on the vibration response of the downstream cylinder until a critical threshold is reached, beyond which this influence diminishes. This behaviour was attributed to modifications in vortex strength within the wake. The Reynolds number strongly influences both the vibration amplitude and the dominant frequency of the downstream cylinder (Lin *et al.* 2020, 2024), as well as its sensitivity to fluid forces (Carberry *et al.* 2001). Similar to the VIV forever of a single cylinder, a finite vibration amplitude also exists in the WIV response of a tandem-cylinder system as $U_r = \infty$, as experimentally demonstrated by Assi *et al.* (2013). However, Assi *et al.* (2013) did not conduct an in-depth analysis of the critical mass ratio. Infinite reduced velocity conditions for either the VIV of a single cylinder or the WIV of tandem cylinders are typically achieved by eliminating the mechanical spring, resulting in zero structural stiffness ($K = 0$) and thus $U_r = \infty$, which is consistent with the methodology adopted in the present study.

Existing studies have established that the mass ratio m^* plays a central role in the dynamic responses of both VIV and WIV systems. In single-cylinder VIV, decreasing m^* broadens the lock-in range and, when $m^* < m^*_{cr}$, leads to sustained large-amplitude oscillations at infinite reduced velocity. However, for WIV, whether an analogous critical mass ratio m^*_{cr} exists and how it depends on wake interference effects remain unclear. The presence of unsteady wake interactions introduces additional flow instabilities and mode coupling, which may fundamentally modify the transition between quiescent and vibrating states, particularly for extreme-light (EL) structures. Clarifying this issue is important not only for advancing the theoretical understanding of wake–structure interactions, but also for engineering applications. Multi-cylinder arrangements are ubiquitous in offshore risers, heat-exchanger tube bundles and marine structural arrays. To address these issues, the present study systematically investigates the WIV of an EL downstream cylinder placed behind an upstream fixed cylinder. By varying m^* and L/D over a wide parameter range, we identify the vibration-regime boundaries, determine the existence and variation of the critical mass ratio m^*_{cr} under unsteady wakes and analyse the associated flow-field dynamics responsible for the transition between non-vibrating and sustained-vibration states. The remainder of this paper is organised as follows. The numerical methodology and validation are presented in § 2. The critical mass ratio and the corresponding physical mechanisms are discussed in § 3. The vibration-frequency characteristics and the dependence of the response on reduced velocity are examined in § 4. Finally, the main conclusions are summarised in § 5.

2. Problem formulation

2.1. *Physical model*

The configuration of the tandem cylinder system is illustrated in figure 1. The downstream EL cylinder, with diameter D, undergoes purely transverse oscillations in the wake of the upstream cylinder. The structural damping is set to zero to maximise the vibration amplitude. The Reynolds number is fixed at 60, with a focus on the system response under reduced velocity $U_r = \infty$ (defined as $U_r = 2\pi U_0/(\omega_n D)$, where U_0 denotes the free-stream velocity and ω_n is the natural frequency). The infinite reduced velocity condition is achieved by setting the system stiffness K to zero. The spacing ratio L/D is varied from 1.1 to 6.0. Within this range of L/D and at the selected Reynolds number, the flow field around the fixed tandem cylinders undergoes a transition from steady to unsteady

https://doi.org/10.1017/jfm.2026.11941 Published online by Cambridge University Press

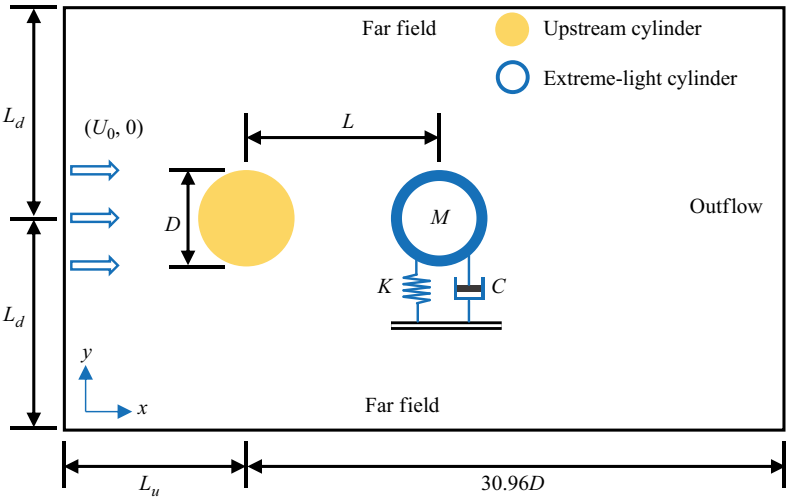


Figure 1. Schematic of the EL-cylinder WIV system. Here L_d represents the distance from the upstream cylinder to the lateral boundary, and L_u denotes the distance from the upstream cylinder to the inlet boundary.

behaviour, highlighting the influence of the mass ratio m^* on flow-field stability. The mass ratio m^* is varied from 0.2 to 14 to identify the critical mass ratio of the EL-cylinder WIV system. The computational domain size, including L_d and L_u, is selected based on domain-size convergence analysis.

2.2. *Methodology*

2.2.1. *Numerical methods*

The fluid flow is governed by the two-dimensional Navier–Stokes (N–S) equations, including the conservation of mass and momentum, as follows:

$$\nabla \cdot \boldsymbol{u} = 0, \tag{2.1}$$

$$\frac{\partial \boldsymbol{u}}{\partial t} + \boldsymbol{u} \cdot \nabla \boldsymbol{u} = -\nabla p + \frac{1}{Re}\nabla^2 \boldsymbol{u} + \boldsymbol{f}, \tag{2.2}$$

where the velocity $\boldsymbol{u}$ and pressure p are non-dimensionalised by U_0 and $\rho_0 U_0^2$, respectively. Other physical quantities, lengths and time are non-dimensionalised by D and D/U_0, respectively, with $t = TU_0/D$. Note that the force term $\boldsymbol{f}$ in (2.2) is the Eulerian force, used to impose the no-slip boundary condition for the immersed boundary method.

The interaction between the fluid and the solid via the immersed boundary method can be calculated by the feedback law (Kim *et al.* 2002; Huang *et al.* 2007). The Lagrangian forcing $\boldsymbol{F}$ is calculated by the penalty approach:

$$\boldsymbol{F} = \kappa \int_0^t (\boldsymbol{U}_{ib} - \boldsymbol{U})\, \mathrm{d}t' + \psi(\boldsymbol{U}_{ib} - \boldsymbol{U}), \tag{2.3}$$

where κ and ψ are large negative free constants, $\boldsymbol{U}$ is the velocity of the immersed solid Lagrangian point and $\boldsymbol{U}_{ib}$ is the fluid velocity interpolated on the immersed boundary point, expressed as

$$\boldsymbol{U}_{ib}(s, t) = \int_\Omega \boldsymbol{u}(\boldsymbol{x}, t)\delta(\boldsymbol{X}(s, t) - \boldsymbol{x})\, \mathrm{d}\boldsymbol{x}, \tag{2.4}$$

https://doi.org/10.1017/jfm.2026.11941 Published online by Cambridge University Press

with $\delta()$ denoting the Dirac delta function in x and y directions, defined as

$$\delta(x) = \frac{1}{h^2}\phi\left(\frac{x}{h}\right)\phi\left(\frac{y}{h}\right), \tag{2.5}$$

where h denotes the grid spacing. The four-point delta function $\phi(r)$ is used, defined as

$$\phi(r) = \begin{cases} \frac{1}{8}(3 - 2\,|r|) + \sqrt{1 + 4\,|r| - 4r^2}, & 0 \le |r| < 1, \\ \frac{1}{8}(5 - 2\,|r|) - \sqrt{-7 + 12\,|r| - 4r^2}, & 1 \le |r| < 2, \\ 0, & 2 \le |r|\,. \end{cases} \tag{2.6}$$

The relationship between the Lagrangian force and the Eulerian force is given by

$$\boldsymbol{f}(\boldsymbol{x}, t) = \int_{\Gamma} \boldsymbol{F}(\boldsymbol{X}, t)\delta(\boldsymbol{x} - \boldsymbol{X})\,\mathrm{d}\boldsymbol{X}. \tag{2.7}$$

The downstream EL cylinder is allowed to oscillate passively in the y direction under the action of the fluid flow. The governing equation is given as follows:

$$M\ddot{Y} + C\dot{Y} + KY = F_y, \tag{2.8}$$

where M, C and K are the structural mass, damping and stiffness, respectively, $\ddot{Y}$, $\dot{Y}$ and Y are the acceleration, velocity and displacement of the downstream EL cylinder, F_y is the fluid force acting on a cylinder in the y direction, the sum of vortex force F_{vortex} and potential added-mass force $F_{potential} = -[C_A M_f \ddot{Y}]$, and C_A is the potential added-mass coefficient equal to 1. The equation can be dimensionless by introducing the following dimensionless parameters:

$$\begin{gathered} y = Y/D, \qquad m^* = 4M/(\pi\rho D^2), \quad C_y = 2F_y/(\rho U^2 D), \\ U_r = 2\pi U_0/(\omega_n D), \quad \omega_n = \sqrt{K/M}, \qquad \zeta = C/(2M\omega_n). \end{gathered} \tag{2.9}$$

Combining (2.8) and (2.9) yields the dimensionless equation for the downstream EL cylinder:

$$\ddot{y} + \frac{4\pi\zeta}{U_r}\dot{y} + \left(\frac{2\pi}{U_r}\right)^2 y = \frac{2C_y}{\pi m^*}. \tag{2.10}$$

2.2.2. *The flow solver*

The N–S equations are discretised as

$$D\boldsymbol{u}^{n+1} = 0, \tag{2.11}$$

$$\frac{\boldsymbol{u}^{n+1} - \boldsymbol{u}^n}{\Delta t} + N\boldsymbol{u}^{n+1} = -Gp^{n+\frac{1}{2}} + \frac{1}{2Re}(L\boldsymbol{u}^{n+1} + L\boldsymbol{u}^n) + f^n, \tag{2.12}$$

where N, G, L and D are the linearised discrete convective operator, the discrete gradient operator, the discrete Laplacian operator and the discrete divergence operator, respectively. The N–S equations are solved by the fractional step method on a staggered Cartesian grid. The velocity components and momentum forcing are defined on the staggered grid, whereas the pressure is applied at the centres of cells. Fully implicit time advancement is employed, with the Crank–Nicholson scheme being used for the discretisation of the diffusion and convection terms. Decoupling of the velocity and pressure is achieved by

https://doi.org/10.1017/jfm.2026.11941 Published online by Cambridge University Press

block LU decomposition in conjunction with approximate factorisation. Details of the approximate factorisation can be found in Kim *et al.* (2002) and Huang *et al.* (2007). In summary, it can be written as

$$\frac{\boldsymbol{u}^* - \boldsymbol{u}^n}{\Delta t} + N\boldsymbol{u}^* = -Gp^{n-1/2} + \frac{1}{2Re}(L\boldsymbol{u}^* + L\boldsymbol{u}^n) + f^n, \tag{2.13}$$

$$\Delta t DG\delta p = D\boldsymbol{u}^*, \tag{2.14}$$

$$\boldsymbol{u}^{n+1} = \boldsymbol{u}^* - \Delta t G\delta p, \tag{2.15}$$

$$p^{n+1/2} = p^{n-1/2} + \delta p, \tag{2.16}$$

where $\boldsymbol{u}^*$ denotes the intermediate velocity. Due to the implicit treatment of the nonlinear convection terms, further decoupling of the intermediate velocity components is made and finally a system of tridiagonal matrices is formed instead of a large sparse matrix. The momentum equation is then solved directly without iteration, and the computational cost is reduced significantly. The pressure Poisson equation is solved by a direct method using Fast Fourier transform or a multi-grid method. The pressure is then used to correct the velocity field to satisfy the continuity equation.

2.2.3. *Discretisation of the cylindrical governing equations*

When solving (2.10), the cylinders with an extremely small m^* are prone to numerical instability due to added-mass effects. We propose a simple strategy based on the Newmark-β method and the centre difference format (Belanger *et al.* 1995; Yvin *et al.* 2018; Han *et al.* 2025) for solving the dynamical equations with extremely small m^*. Considering the dimensionless governing equation at time $t + \Delta t$, the term $(\pi/2)\ddot{y}_{t+\Delta t}$ is added to both sides of (2.10), yielding

$$\left(\frac{\pi}{2} + 1\right)\ddot{y}_{t+\Delta t} + \frac{4\pi\zeta}{U_r}\dot{y}_{t+\Delta t} + \left(\frac{2\pi}{U_r}\right)^2 y_{t+\Delta t} = \frac{2C_y^{t+\Delta t}}{\pi m^*} + \frac{\pi}{2}\ddot{y}_{t+\Delta t}. \tag{2.17}$$

Performing the centre difference format for the acceleration term on the right-hand side of the equation, we can obtain

$$\left(\frac{\pi}{2} + 1\right)\ddot{y}_{t+\Delta t} + \frac{4\pi\zeta}{U_r}\dot{y}_{t+\Delta t} + \left(\frac{2\pi}{U_r}\right)^2 y_{t+\Delta t} = \frac{2C_y^{t+\Delta t}}{\pi m^*} + \pi\frac{(\Delta t\dot{y}_{t+\Delta t} - y_{t+\Delta t} + y_t)}{\Delta t^2}. \tag{2.18}$$

Based on the linear acceleration assumption of the Newmark-β method, the expressions for the acceleration and velocity at time $t + \Delta t$ are obtained:

$$\ddot{y}_{t+\Delta t} = \frac{1}{\beta\Delta t^2}(y_{t+\Delta t} - y_t) - \frac{1}{\beta\Delta t}\dot{y}_n - \left(\frac{1}{2\beta} - 1\right)\ddot{y}_n, \tag{2.19}$$

$$\dot{y}_{t+\Delta t} = \frac{\alpha}{\beta\Delta t}(y_{t+\Delta t} - y_t) + \left(1 - \frac{\alpha}{\beta}\right)\dot{y}_n - \left(\frac{\alpha}{2\beta} - 1\right)\Delta t\ddot{y}_n. \tag{2.20}$$

According to previous research (Wang *et al.* 2020*b*), the values of α and β are set to 0.5 and 0.25, respectively. Based on (2.18)–(2.20), the acceleration, velocity and displacement at time $t + \Delta t$ are obtained. Details of the present two-way coupling solver can be found in Huang *et al.* (2007).

https://doi.org/10.1017/jfm.2026.11941 Published online by Cambridge University Press

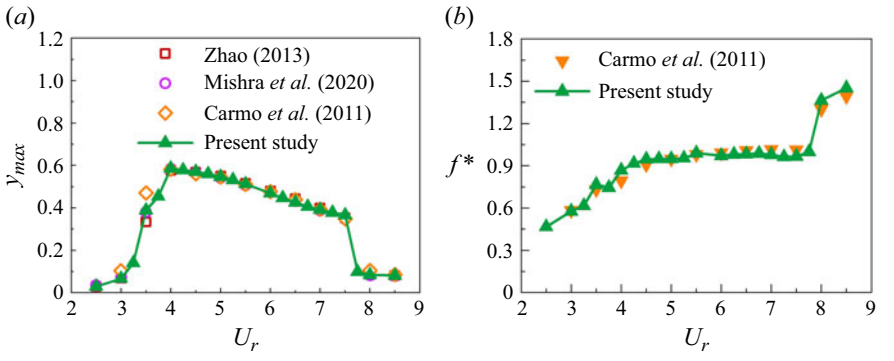


Figure 2. Validation of flow past a circular cylinder with a mechanical spring at $Re = 150$ and $m^* = 2.546$. (*a*) Vibration amplitudes. (*b*) Vibration frequency.

2.3. *Validations*

The computational fluid domain has dimensions of $40.96D$ in the streamwise direction and $30D$ in the transverse direction, with the centre of the upstream cylinder located $10D$ downstream of the inlet boundary and $15D$ from both the upper and lower boundaries. The fluid computational domain depicted in figure 1 is discretised into 2049 uniform Eulerian grid points along the x direction. Along the y direction, a uniform Eulerian grid is maintained over $y \in [-4, 4]$, with gradual stretching applied beyond this range. This strategy results in a total of 1 436 349 computational nodes. To ensure consistent resolution coupling between the fluid and structural domains, the Lagrangian grid on the cylinder consists of 157 points. The grid resolution, time-step size ($\Delta t = 0.003$) and domain size were determined through systematic convergence studies, as detailed in Appendix A. The in-house solver used in this study has been previously validated in various applications related to fluid–structure interactions (Huang *et al.* 2007; Huang & Sung 2009; Huang & Sung 2010; Uddin *et al.* 2015; Han *et al.* 2025). For completeness, we further validate the numerical method against the VIV response of a single cylinder. Key parameters align with established benchmarks: Reynolds number $Re = 150$ and mass ratio $m^* = 2.546$, consistent with prior studies (Carmo *et al.* 2011; Zhao 2013; Mishra *et al.* 2020). Comparative results in figure 2 show excellent agreement between simulated and literature-reported maximum amplitude and frequency ratio characteristics within the lock-in region. It should be noted that fluid–structure interaction simulations at extremely low mass ratios are highly sensitive to the added-mass effect, which can induce numerical instability in conventional partitioned coupling algorithms. Further validation examines the m^*-dependent VIV response under $U_r = \infty$, with results presented in figure 3(*a*). The vibration amplitudes show good agreement with previous studies across various m^* values (Bourguet 2023). The minor discrepancies with published results (Navrose & Mittal 2017; Shiels *et al.* 2001) may arise from differences in numerical schemes and treatment of the added-mass coupling. In addition, the vibration responses of rigidly connected cylinders under $U_r = \infty$ are compared with Yu *et al.* (2025), as shown in figure 3(*b*). The results show excellent agreement, further demonstrating the effectiveness of the proposed numerical method. Additionally, fixed tandem cylinder configurations are validated against published results in table 1, demonstrating good agreement in hydrodynamic force coefficients. These validations confirm the robustness and predictive accuracy of the simulation method.

https://doi.org/10.1017/jfm.2026.11941 Published online by Cambridge University Press

References	$C_{D1,mean}$	$C_{D2,mean}$	$C_{L1,rms}$	$C_{L2,rms}$	St
Alam (2016)	1.018	−0.13	0.022	0.212	0.125
Meneghini *et al.* (2001)	1.0	−0.08	—	—	0.125
Mahír & Altaç (2008)	1.05	−0.56	0.020	0.191	0.13
Koda & Lien (2013)	1.04	−0.129	0.016	0.212	0.127
Present	1.015	−0.124	0.0202	0.208	0.125

Table 1. Validation for the fixed tandem cylinder at $L/D = 3$ and $Re = 200$.

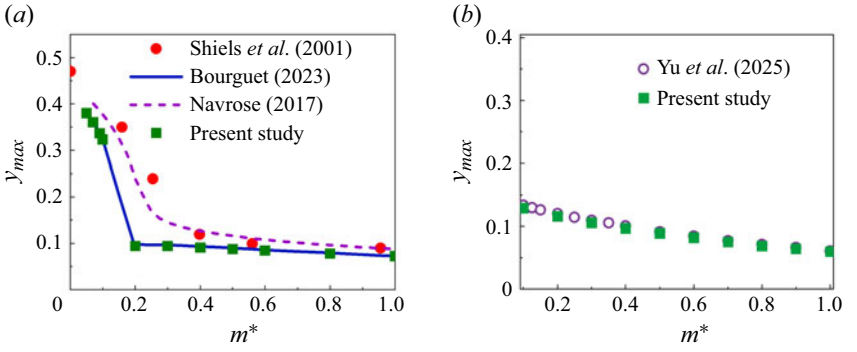


Figure 3. Validation of flow past (*a*) a freely vibrating cylinder without mechanical spring force at $Re = 100$ and (*b*) rigidly connected cylinders without mechanical spring force at $L/D = 2.0$ and $Re = 150$.

3. Results

3.1. *Classification of flow mode*

After validating the mesh resolution, time step and numerical methodology, the simulation scheme is employed to investigate the EL-cylinder WIV responses over a range of spacing ratios (L/D) and mass ratios (m^*). Figure 4 presents a comprehensive classification of the flow regimes observed within the L/D–m^* parameter space, along with representative vorticity fields for each regime. Compared with a single-cylinder system, the flow characteristics of the fixed tandem cylinders are considerably more complex due to inter-cylinder interference effects. The gap flow exhibits distinct flow modes at different L/D values (Zdravkovich 1987; Sumner 2010): (i) the overshoot regime ($1 < L/D < 1.2$–1.8), in which the shear layers from the upstream cylinder pass directly across the downstream EL cylinder before undergoing periodic vortex shedding; (ii) the reattachment regime (1.2–$1.8 < L/D < 3.4$–3.8), where the upstream shear layers reattach to the surface of the EL cylinder; and (iii) the co-shedding regime ($L/D > 3.8$), in which vortices are shed synchronously from both the upstream cylinder and EL cylinder. Based on the dynamic interactions between the EL cylinder and the shear layers originating from the upstream cylinder, five distinct flow regimes are identified: (i) alternating reattachment (AR), (ii) combined overshoot and weak alternating reattachment (COWAR), (iii) overshoot (OS), (iv) co-shedding (CS), and (v) steady flow. These regimes are colour-coded in figure 4 for clarity. In the AR regime, shear layers from the upstream cylinder periodically reattach to the EL-cylinder surface. The COWAR regime, a newly identified flow mode occurring at small mass and spacing ratios, is characterised by weak vortices within the gap region. In both the COWAR and OS regimes, the primary shear layers from the upstream cylinder traverse the EL cylinder, forming alternating vortex streets. The CS regime occurs at

https://doi.org/10.1017/jfm.2026.11941 Published online by Cambridge University Press

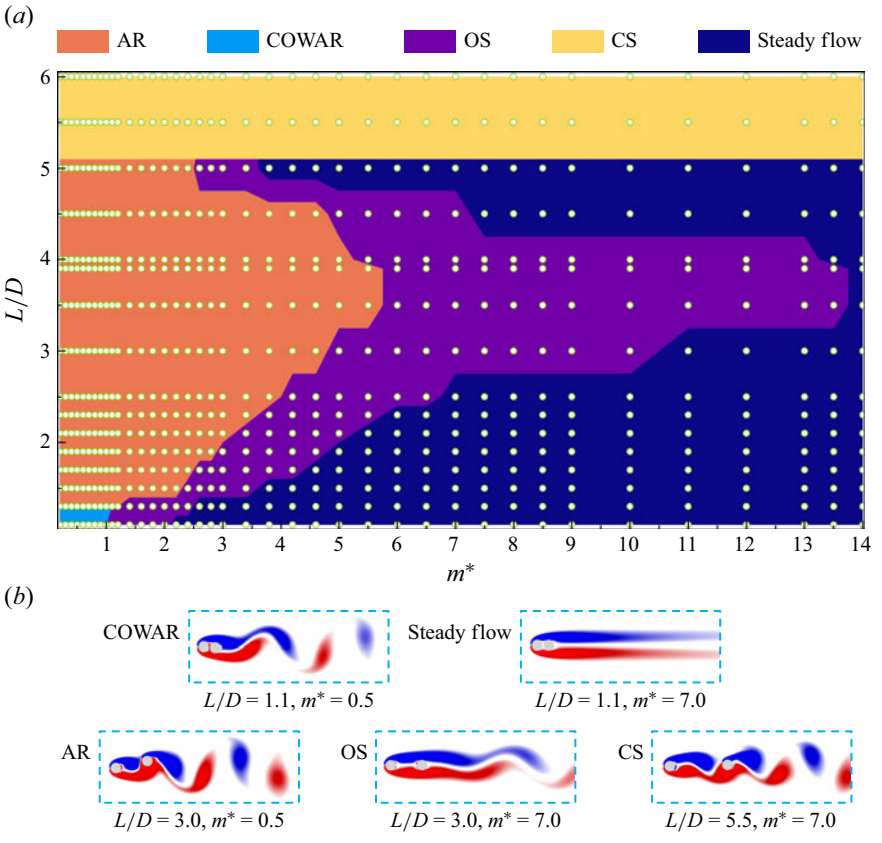


Figure 4. (*a*) Flow regime classification and (*b*) vorticity fields of the EL-cylinder WIV in the L/D–m^* parameter space. The coloured regions indicate AR (alternating reattachment), OS (overshoot), COWAR (combined overshoot and weak alternating reattachment), CS (co-shedding) and steady flow regimes.

larger L/D values, where the shear layers from the upstream cylinder are fully developed, allowing simultaneous vortex shedding from both cylinders. In the steady flow regime, the EL cylinder remains stationary. The flow regime classification indicates strong fluid–structure energy transfer in the AR, COWAR and CS regimes, which is consistent with the observed pronounced vibration responses.

3.2. *Vibration response*

This section presents a comprehensive analysis of the vibration response characteristics to determine the critical mass ratio (m^*_{cr}) of the EL-cylinder WIV system. To quantify the vibration amplitude, y_{10} – defined as the average of the top 10 % peak amplitudes – is adopted as the representative response metric, following established methodologies (Han *et al.* 2023*a*,*b*). While conventional frequency analysis typically examines the ratio of the structural vibration frequency to the natural frequency (Zhang *et al.* 2022), this approach becomes invalid when the natural frequency loses its physical meaning due to zero stiffness ($K = 0$). Consequently, a modified frequency ratio is introduced as f^*/f_s, where f^* denotes the dominant frequency extracted from the time-history signals of the cylinder (displacement or lift force) and f_s represents the vortex-shedding frequency of a fixed single cylinder at the same Reynolds number. Both f^* and f_s are obtained using the fast Fourier transform algorithm.

https://doi.org/10.1017/jfm.2026.11941 Published online by Cambridge University Press

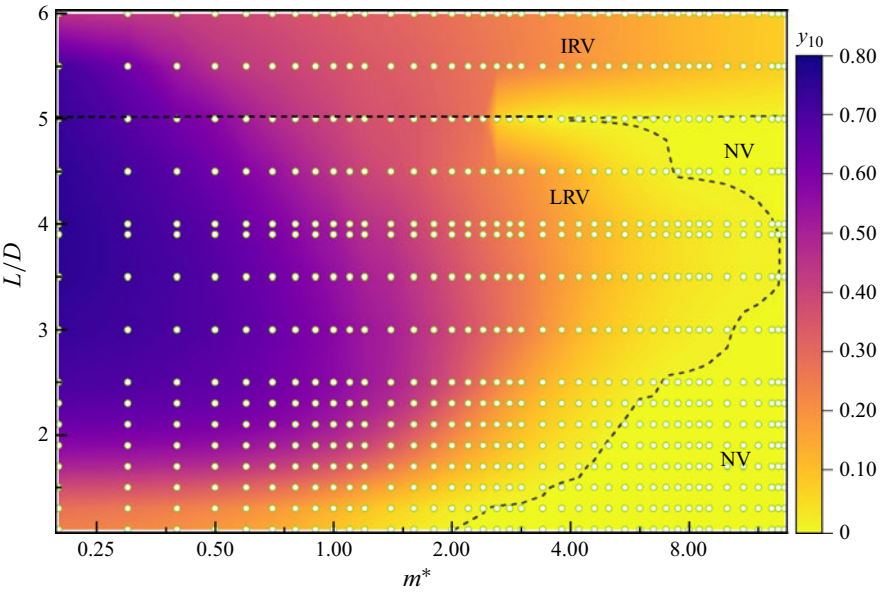


Figure 5. Vibration responses and vibration-regime classification of the EL-cylinder WIV within the L/D–m^* parameter space. Here LRV denotes the limited-range vibration regime, NV denotes the non-vibration regime and IRV denotes the infinite-range vibration regime.

Figure 5 illustrates the amplitude response characteristics of the downstream EL cylinder within the L/D–m^* parameter space. For a given L/D, increasing the mass ratio m^* leads to a reduction in vibration amplitude. When $1.1 \leq L/D < 5.5$, the amplitude y_{10} gradually decreases to zero as m^* increases. In contrast, for $L/D \geq 5.5$, the vibration amplitude does not diminish to zero, even at large mass ratios. Based on the vibration responses observed in the L/D–m^* parameter space, the vibration characteristics can be classified into three regimes: (1) the limited-range vibration (LRV) regime, in which cylinder vibration occurs only within a finite range of m^* and the amplitude decreases to zero as m^* increases; (2) the infinite-range vibration (IRV) regime, where cylinder vibration persists within the investigated m^* range with a non-zero amplitude; and (3) the non-vibration (NV) regime, characterised by a steady flow field with $y_{10} = 0$. As shown in figure 5, a critical mass ratio m^*_{cr} exists for the EL cylinder under the influence of an unsteady wake, marking the transition from the LRV regime to the NV regime. The value of m^*_{cr} exhibits a strong dependence on the spacing ratio L/D. Specifically, when $1.1 \leq L/D < 3.9$, m^*_{cr} increases with increasing L/D; beyond this range, m^*_{cr} decreases rapidly as L/D increases. This transition is closely related to the vortex formation length of a single cylinder (see figure 17 in Appendix B), where the vortex formation length, $L_f/D = 3.9$, coincides with the critical spacing ratio. In fact, the vortex formation location of a single cylinder determines the region in the upstream wake with the most stable vortex structures and the strongest circulation intensity as the spacing ratio of tandem cylinders increases (Gerrard 1966; Griffin & Ramberg 1974). When the EL cylinder is located near this region, the influence of the upstream cylinder wake is maximised, leading to a larger m^*_{cr} value. As the EL cylinder moves away from this region, the enhancing effect of the upstream wake gradually weakens, and m^*_{cr} correspondingly decreases. When $m^* > m^*_{cr}$, the system reaches a stable state, consistent with the steady flow regime shown in figure 4. Compared with the 'VIV forever' phenomenon observed in single-cylinder systems at

https://doi.org/10.1017/jfm.2026.11941 Published online by Cambridge University Press

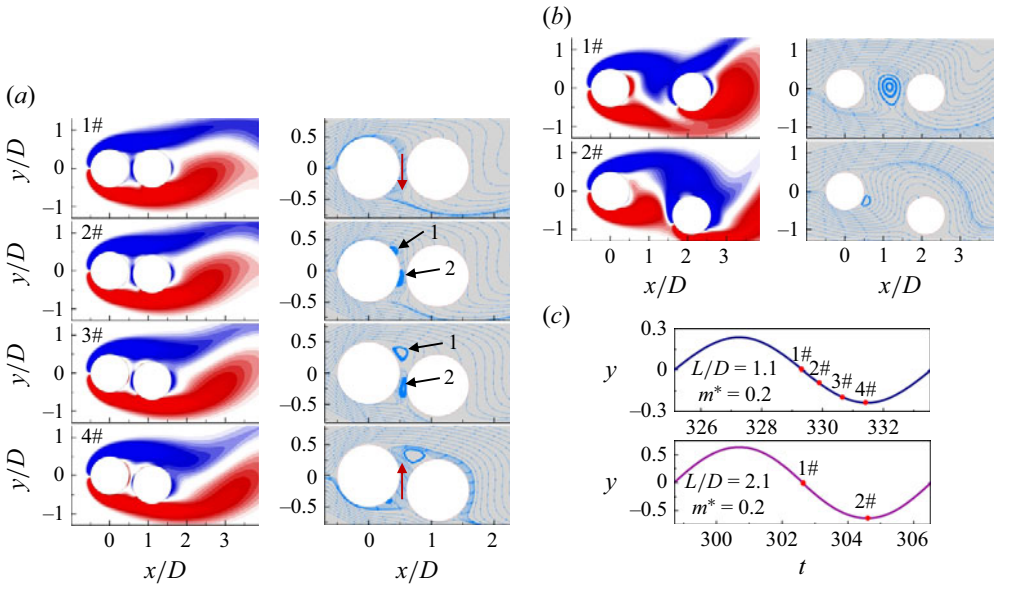


Figure 6. Instantaneous vorticity and streamlines over one-quarter period at (*a*) $L/D = 1.1$, $m^* = 0.2$ and (*b*) $L/D = 2.1$, $m^* = 0.2$; (*c*) time-history amplitude. Red arrows indicate gap-flow direction.

$m^* < m^*_{cr}$, the vibration characteristics of the EL cylinder are significantly altered by the presence of an unsteady wake. Experiments by Govardhan & Williamson (2002) demonstrated that, in single-cylinder VIV, the cylinder undergoes an abrupt transition from a near-stationary state to large-amplitude vibration once m^* falls below m^*_{cr}. In contrast, with an upstream cylinder present, the EL cylinder exhibits a smooth transition in vibration amplitude rather than an abrupt change near m^*_{cr}. Furthermore, Li *et al.* (2018) investigated the WIV response at $L/D = 2$ and $Re = 60$, and reported weak vibration at $m^* = 5$ under high reduced velocity, which is consistent with the present prediction of m^*_{cr}. It should be noted that variations in system parameters, such as the Reynolds number, will also lead to changes in the critical mass ratio of the system. The following section further examines the fluid–structure interaction mechanisms underlying these vibration regimes.

3.2.1. *Transition from LRV regime to NV regime*

Figure 5 shows that, in the LRV regime, the vibration amplitude of the downstream EL cylinder gradually diminishes to zero with increasing m^*. The NV regime corresponds to a zero-amplitude response associated with a steady flow regime (see figure 4). The LRV regime encompasses three flow modes: AR, COWAR and OS. For $L/D \leq 1.3$, the vibration amplitudes remain relatively small (e.g. $y_{10} = 0.28$ at $L/D = 1.3$ and $m^* = 0.2$). At the same mass ratio, increasing L/D to 2.1 results in an abrupt increase in amplitude to 0.68, followed by a gradual rise to 0.74 at $L/D = 3.0$. Meanwhile, the boundary of m^*_{cr} range expands significantly, from $m^* \leq 2$ at $L/D = 1.1$ to $m^* \leq 13.5$ at $L/D = 3.5$, which correlates closely with transitions among the flow regimes. Figure 6 presents transient flow snapshots at $L/D = 1.1$ and 2.1 for $m^* = 0.2$. Owing to the periodicity of the flow, only one-quarter of a vibration cycle is shown. In the COWAR regime, the shear layers separated from the upstream cylinder bypass the EL cylinder, forming alternating shedding vortices. Unlike the gap-flow dynamics observed in the OS mode (Zhu *et al.* 2019, 2021), small vortices shed from the upstream cylinder – barely discernible in the vorticity contours – induce a reversal of the gap flow between moments 2# and 3#. Vortex

https://doi.org/10.1017/jfm.2026.11941 Published online by Cambridge University Press

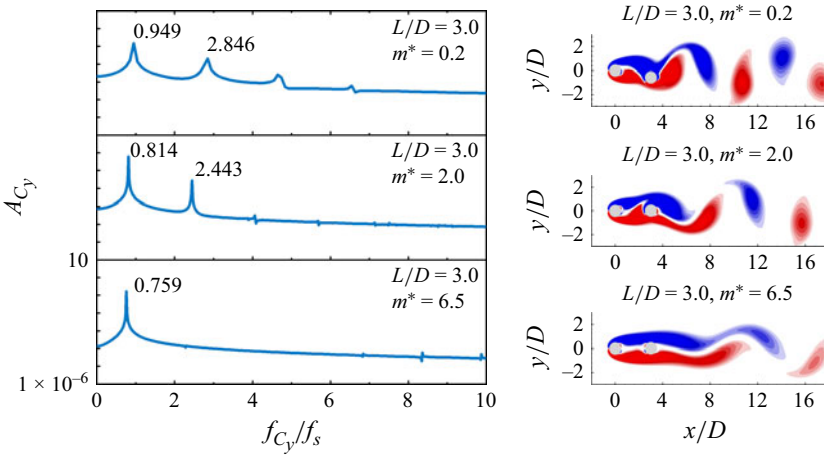


Figure 7. Transverse force coefficient spectra and corresponding vorticity fields at $L/D = 3.0$ for different m^*.

2 dissipates upon impinging on the EL cylinder, whereas vortex 1 persists and attracts the gap flow. In the AR regime (figure 6*b*), the elongated shear layers promote alternating reattachment onto the EL-cylinder surface. The relatively small vortex in the COWAR regime limits its ability to modify the gap flow, and the stable shear layers surrounding the EL cylinder suppress vibration responses, thereby explaining the weak EL-cylinder WIV responses observed at small L/D.

As L/D increases further, a transition to the AR regime occurs. Figure 7 presents the spectral analysis of the transverse force coefficients together with vorticity contours at $L/D = 3.0$ for $m^* = 0.2$, 2.0 and 6.5, illustrating the transition from the AR to the OS regime. At $m^* = 0.2$, pronounced high-order frequency components appear in the spectra, indicating strong interactions between the cylinder motion and the shear layers; this is accompanied by shear-layer attachment to the surface of the downstream EL cylinder in the vorticity field. Increasing m^*, these high-order force components gradually weaken and ultimately vanish in the OS regime. Notably, at $m^* = 6.5$, only a single dominant frequency remains, corresponding to vortex shedding from the downstream EL cylinder. The presence of stable shear layers on both sides of the cylinder effectively suppresses vibration responses.

To further elucidate the fluid–structure interaction characteristics and the associated energy transfer mechanisms in the LRV and NV regimes, representative cases are analysed using dynamic mode decomposition (DMD). The dataset consists of at least 350 consecutive flow-field snapshots sampled at $\Delta t = 0.15$ from the fully developed flow. The flow-field region for DMD analysis is defined by $x/D \in [0.51, 15]$ and $y/D \in [y_c - 4, y_c + 4]$, where y_c denotes the lateral coordinate of the cylinder centre. The DMD analysis is applied to both vorticity and pressure fields to extract the dominant modal structures and their corresponding energy contributions. The modal decomposition procedure follows established mathematical formulations (Xu *et al.* 2023). When dealing with moving cylinder boundaries, the traditional DMD technique may produce spurious structures in the modal results due to the alternating occupation of certain mesh grids by the fluid and solid domains. To avoid this issue, the centre of the EL cylinder is taken as the reference frame, and a coordinate transformation is performed on the flow field (Menon & Mittal 2020), thereby converting the instantaneous flow field into a reference coordinate system consistent with that of the EL cylinder. The stability of each mode is determined

https://doi.org/10.1017/jfm.2026.11941 Published online by Cambridge University Press

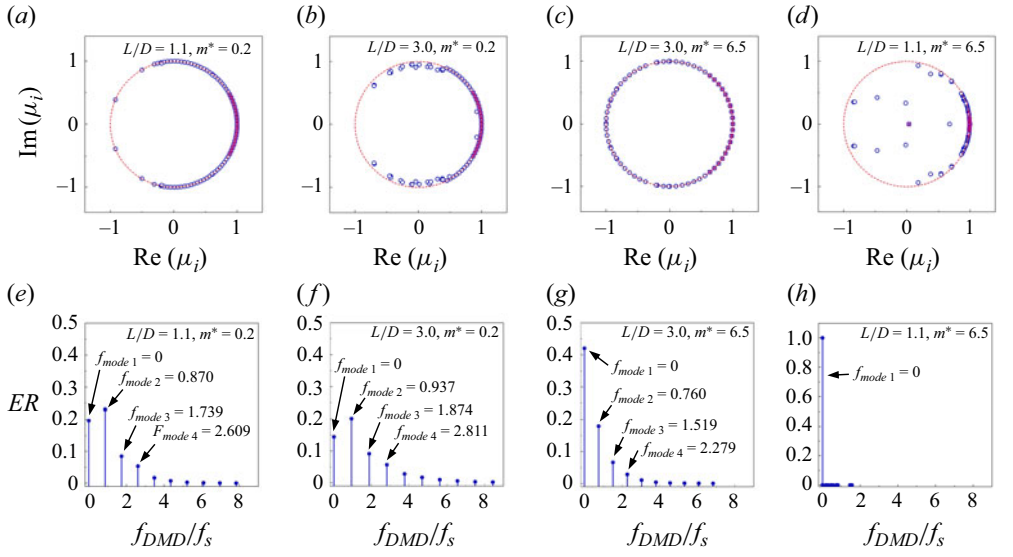


Figure 8. (*a–d*) Ritz eigenvalue spectra at different L/D and m^*, where the cross symbols denote the eigenvalues of the first ten modes; (*e–h*) modal energy distributions of the first ten modes.

by the location of its Ritz eigenvalue: eigenvalues lying on the unit circle correspond to periodic modes, those inside the circle indicate stable modes and those outside the circle represent unstable modes. Unlike the conventional DMD implementations where modes are normalised to unit norm and modal amplitudes are used to characterise modal energy, at present the modal contribution is evaluated directly from the original mode magnitude and temporal coefficients following Xu *et al.* (2023). The energy ratio of mode j is defined as

$$ER_j = \frac{E_j}{\sum_{j=1}^{r} E_j}, \tag{3.1}$$

where E_j denotes the modal energy of the jth mode, and the importance of the jth mode is quantified by the energy ratio ER.

Figure 8 presents the Ritz eigenvalue spectra and the modal energy ratios of the first ten modes. The complex eigenvalues appear in conjugate pairs; here, only eigenvalues with non-negative imaginary parts are used to calculate the DMD frequencies. Mode 1 represents the time-averaged mode with $f_{DMD}/f_s = 0$, mode 2 corresponds to the Kármán vortex street mode and mode 3 and higher-order modes represent harmonic modes (Bagheri 2013). Figure 8(*a–c*,*e–g*) corresponds to the LRV regime, whereas figure 8(*d*,*h*) represents the NV regime. The eigenvalues are primarily distributed along the unit circle (see figure 8*a–d*), indicating that the system dynamics converges to an attractor. In both the COWAR and AR flow regimes (figures 8*e* and 8*f*), the first two modes dominate the dynamics at low mass ratios. Notably, the modal energy of mode 2 exceeds that of mode 1, while the energy associated with higher-order modes decays progressively. As m^* increases, the flow mode transitions to the OS regime ($L/D = 3.0$, $m^* = 6.5$), the energy contribution of the first-order mode increases markedly, reaching $ER \approx 0.42$, which is significantly larger than that of the second-order mode. In the NV regime, corresponding to the steady flow regimes, mode 1 (the time-averaged mode) becomes dominant, as illustrated in figure 8(*h*).

https://doi.org/10.1017/jfm.2026.11941 Published online by Cambridge University Press

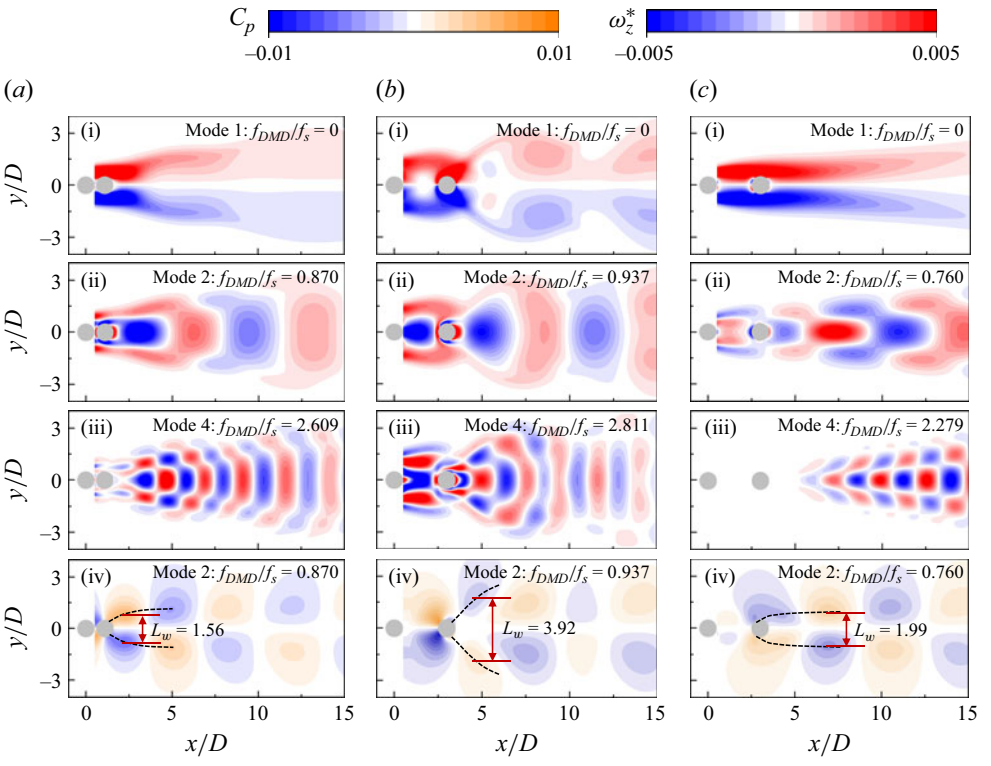


Figure 9. The DMD modes of the vorticity and pressure fields at different L/D and m^*: (*a*) $L/D = 1.1$, $m^* = 0.2$; (*b*) $L/D = 3.0$, $m^* = 0.2$; (*c*) $L/D = 3.0$, $m^* = 6.5$. The black dashed line represents the trajectory of the vortex development, and L_w represents the near-wake modal width, defined as the transverse distance between the two local maxima of the pressure DMD modal magnitude in the near-wake region.

Figure 9 presents the DMD modes of the vorticity and pressure fields under different parameter combinations, corresponding to the cases shown in figure 8(*a–c*). The vortex development trajectories and the near-wake modal width, L_w, are illustrated in the pressure-field modal results. It should be noted that although mode 3 possesses a relatively large energy ratio, it is primarily associated with velocity and drag fluctuations in the streamwise direction; therefore, its contribution to the transverse vibration of the cylinder is relatively limited. This study mainly focuses on modes such as mode 2 and mode 4, which directly influence the transverse force acting on the cylinder. Varying L/D and m^*, the EL-cylinder WIV system exhibits distinctly different modal characteristics. In the COWAR flow regime ($L/D = 1.1$, $m^* = 0.2$; figure 9*a*), the time-averaged shear layer associated with mode 1 directly traverses the EL cylinder. The modal structures of modes 2 and 4 resemble those of a single-cylinder vortex street. Near the EL cylinder, mode 2 exhibits pronounced near-wake characteristics, whereas mode 4 remains relatively weak. Under this flow condition, both mode 1 and mode 2 possess large energy ratios *ER*.

When the spacing ratio increases to the AR flow regime (e.g. $L/D = 3.0$, $m^* = 0.2$; figure 9*b*), the high-gradient shear layer of mode 1 surrounding the EL cylinder shrinks in the streamwise direction and expands in the transverse direction. Although the mode shape of mode 1 exhibits periodic characteristics, it still represents the time-averaged mode. This is because the mesh coordinates are transformed during the DMD preprocessing stage to align with the reference frame of the moving cylinder. Consequently, mode 1

https://doi.org/10.1017/jfm.2026.11941 Published online by Cambridge University Press

corresponds to the time-averaged mode in the transformed coordinate system, rather than the conventional time-averaged mode associated with a stationary cylinder. Compared with the COWAR regime, the modal energy of mode 1 is decreased, indicating that the vortex-shedding-related modes (e.g. mode 2 and mode 4) gain a competitive advantage in the modal dynamics. Modes 2 and 4 exhibit pronounced modal features within the gap region, and the transverse width of the Kármán vortex street mode is larger than that observed in the COWAR regime (see figures 9*a*(iv) and 9*b*(iv)). Previous experiments by Assi *et al.* (2010) demonstrated that unsteady vortices shed from the upstream cylinder play a crucial role in sustaining WIV of the downstream cylinder. Consistent with this observation, in the AR flow regime, the upstream shear layers evolve into intense vortices within the gap, exciting a stronger second-order mode and resulting in elevated modal energy for mode 2. The pronounced modal features of modes 2 and 4 around the EL cylinder indicate that higher-order modes govern the system dynamics, which is consistent with the multiple frequency components observed in the transverse force spectra (see figure 7). Under the AR flow regime, the competitive dominance of mode 2 and the higher-order modes over mode 1 promotes the vibration of the EL cylinder.

With a further increase in m^*, the flow transitions to the OS regime, and the corresponding modal characteristics are shown in figure 9(*c*). In this regime, the time-averaged mode resembles that of the COWAR regime but exhibits more pronounced modal features, with the high-gradient shear layer extending over a broader streamwise direction region. In contrast, the modal characteristics of mode 2 – particularly in the near-wake region – are significantly weaker than those observed in the AR regime. Mode 1 becomes energetically dominant over mode 2 in the modal competition. Under this flow condition, the modal energy ratio (*ER*) of mode 1 is approximately 0.42, which is substantially larger than that of mode 2. Mode 4 displays modal structures further downstream and has a negligible influence on cylinder vibrations. Consequently, the energy ratio of mode 1 increases in the OS regime, suppressing cylinder vibrations and reducing energy transfer between the EL cylinder and the surrounding fluid. These trends are further corroborated by the pressure DMD results (figures 9*a*(iv), 9*b*(iv) and 9*c*(iv)). The second-order pressure mode exhibits an antisymmetric distribution with respect to $y = 0$. In the COWAR and AR flow regimes, high-pressure-gradient structures appear near the EL cylinder, leading to strong fluid–structure interactions and efficient energy transfer between the flow and the cylinder. In contrast, in the OS regime, the pressure gradients near the cylinder are considerably weaker. A more detailed analysis of the energy transfer mechanisms between the fluid flow and the cylinder is presented in § 3.3.

3.2.2. *The IRV regime*

As shown in figure 5, when $L/D > 4$, the critical mass ratio m^*_{cr} decreases rapidly with increasing L/D. For the spacing ratio L/D from 5.0 to 5.5, the vibration response transitions to the IRV regime, in which the flow field is characterised by the CS mode. In the IRV regime, the vibration amplitude decreases gradually with increasing m^* but remains non-zero within the investigated m^* range, indicating the persistent occurrence of WIV. This transition is closely associated with changes in the flow field of fixed tandem-cylinder configurations. Figure 10 shows the variation of the root-mean-square lift coefficient of a fixed downstream cylinder as a function of the spacing ratio at $Re = 60$. The critical spacing ratio L_{cr}/D is identified to lie between $L/D = 5.0$ and 5.5. When the spacing ratio exceeds L_{cr}/D, the flow field becomes unstable, which is consistent with the findings of Li *et al.* (2018). Owing to the shielding effect of the upstream cylinder, the critical Reynolds number for a fixed tandem-cylinder system is higher than that of a single

https://doi.org/10.1017/jfm.2026.11941 Published online by Cambridge University Press

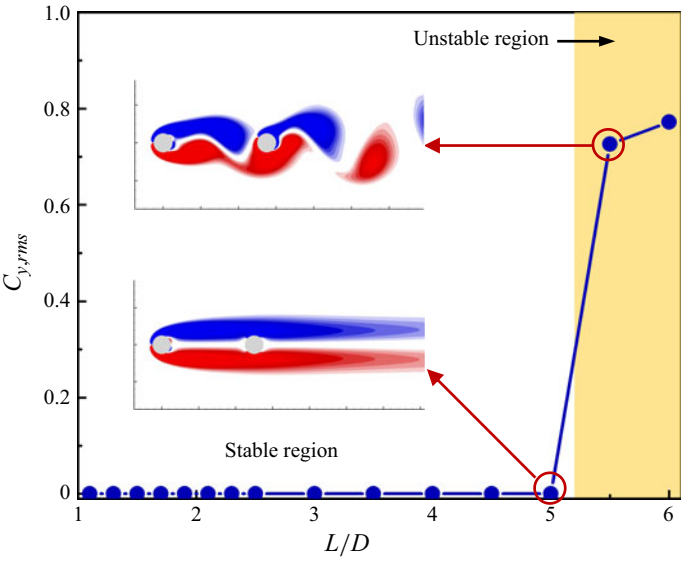


Figure 10. Variation of the root-mean-square lift coefficient of the downstream cylinder with the spacing ratio in fixed tandem cylinders.

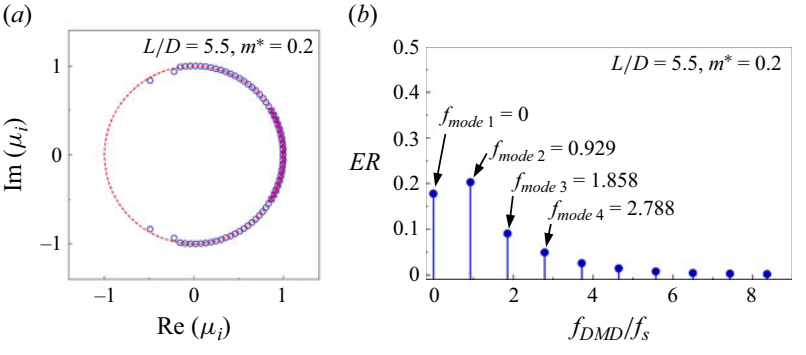


Figure 11. (*a*) Ritz eigenvalue spectrum at $L/D = 5.5$ and $m^* = 0.2$, where the cross symbols denote the eigenvalues of the first ten modes; (*b*) modal energy distribution of the first ten modes.

cylinder ($Re \approx 47$). As the spacing ratio increases, the shielding effect weakens, as does the suppressive influence of the downstream EL cylinder on the wake of the upstream cylinder, ultimately leading to vortex shedding behind both cylinders. In the IRV regime, the EL cylinder is subjected to strong vortex-shedding forces within the mass ratio range, resulting in persistent non-zero vibration amplitudes. To further elucidate the dynamics underlying the IRV regime, representative cases are selected for DMD analysis. Figure 11 presents the Ritz eigenvalue spectra and modal energy ratios of the first ten modes. Most of the eigenvalues lie on the unit circle. Similar to the LRV regime at small m^*, the IRV regime at $L/D = 5.5$ and $m^* = 0.2$ is dominated by the first two modes, while the contributions of higher-order modes decay progressively. Figure 12 presents the DMD modes of both the vorticity and pressure fields. Modes 2 and 4 exhibit pronounced modal structures within the gap region, suggesting that higher-order modes play an important role in governing the system dynamics. In the CS flow regime, fully developed vortices are observed in the gap, enabling mode 2 to maintain its advantage over mode 1 in the competition.

https://doi.org/10.1017/jfm.2026.11941 Published online by Cambridge University Press

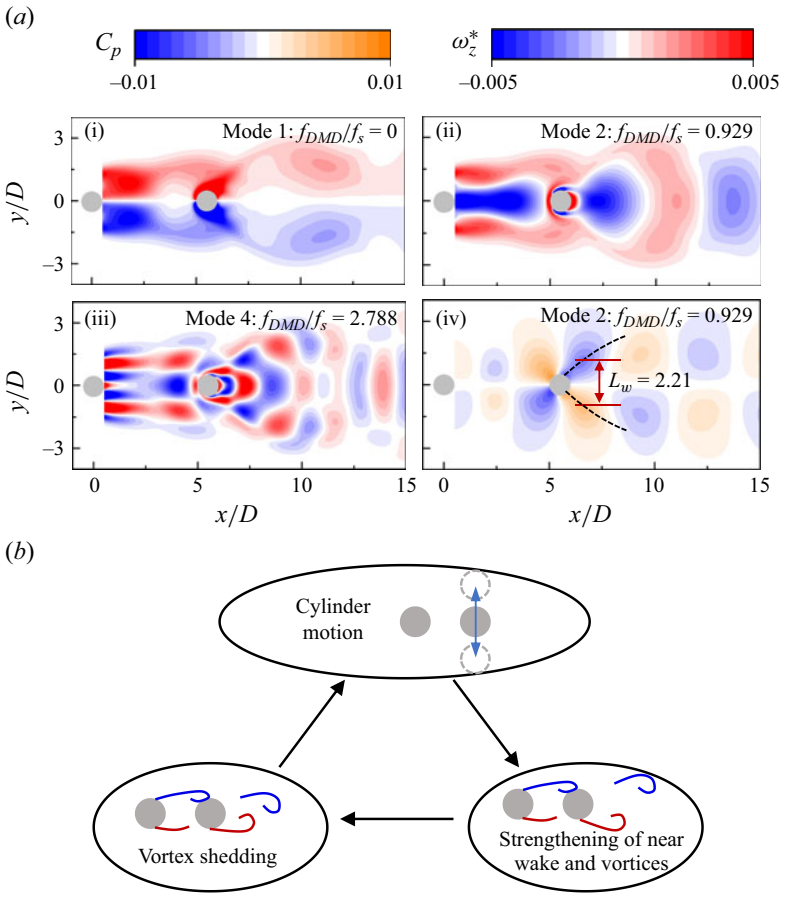


Figure 12. (*a*) The DMD modes of the vorticity and pressure fields at $L/D = 5.5$ and $m^* = 0.2$ in the IRV regime. (*b*) Schematic illustration of the interaction between cylinder motion and vortex shedding. The black dashed line represents the trajectory of the vortex development, and L_w represents the near-wake modal width, defined as the transverse distance between the two local maxima of the pressure DMD modal magnitude in the near-wake region.

The pressure-mode distribution shown in figure 12(*a.iv*) reveals strong pressure-gradient fluctuations on the surface of the EL cylinder, implying intense energy transfer between the cylinder and the surrounding flow. Even at elevated mass ratios, mode 2 maintains a high modal energy ratio *ER*, indicating that the cylinder can sustain vibration with a finite amplitude. This behaviour contrasts with that observed in the LRV regime, where the energy ratio of mode 1 increases progressively with increasing m^*, while the vibration amplitude approaches zero.

The interaction between wake dynamics and EL-cylinder vibration is schematically illustrated in figure 12(*b*). From the above analysis, it is evident that mode 1 and mode 2 are the primary governing modes in both the LRV and IRV regimes. Mode 2 sustains the cylinder vibration at a finite amplitude, whereas the strengthening or weakening of mode 1 determines the vibration amplitude of the cylinder. In the LRV regime, mode 1 does not dominate the EL-cylinder WIV system at low mass ratios, and the cylinder vibrates primarily under the influence of mode 2. The cylinder motion modifies the near-wake characteristics of the EL cylinder, thereby increasing the near-wake modal width and enhancing vortex shedding. The enhanced vortex shedding, in

https://doi.org/10.1017/jfm.2026.11941 Published online by Cambridge University Press

turn, further promotes cylinder vibration, eventually leading to a stable vibration state. As the mass ratio increases, mode 1 gradually becomes the dominant component in the EL-cylinder WIV system, and the cylinder vibration is consequently suppressed. The near-wake width decreases significantly; for example, L_w decreases from 3.92 to 1.99, as shown in figures 9(*b*.iv) and 9(*c*.iv). At the same time, vortex shedding is weakened, as shown in figure 9(*c*.ii). In the IRV regime, however, the continuous influence of the gap flow prevents mode 1 from dominating the EL-cylinder WIV system, while mode 2 consistently maintains a significant modal energy level. This forms a positive feedback cycle between enhanced cylinder vibration and intensified near-wake dynamics, thereby sustaining finite-amplitude vibrations.

3.3. *Energy transfer characteristics*

In § 3.2, the modal characteristics of the EL-cylinder WIV system were analysed, revealing that mode 1 and mode 2 are the dominant modes governing the system dynamics. This section further investigates the energy-transfer process in the EL-cylinder WIV system. First, the work done on the system by the transverse force component, $C_{y,m2}$, corresponding to mode 2 is analysed. For cylinders with low mass ratios, the added-mass effect is an important factor influencing the system response, and the work associated with the added-mass force is therefore also a key focus of this section. The transverse force, F_y, acting on the cylinder is decomposed into two components: the potential force, $F_{potential}$, and the vortex force, F_{vortex}, expressed as follows (Williamson & Govardhan 2008):

$$F_y = F_{potential} + F_{vortex}. \tag{3.2}$$

Non-dimensionalising all force components by $0.5\rho U_{in}^2 DL$ yields

$$C_y = C_{potential} + C_{vortex}, \tag{3.3}$$

where $C_{potential} = -(\pi/2)\ddot{y}$. To quantify the effects of these two components, the corresponding power inputs are defined as P_P and P_V, respectively, as follows:

$$P_P = -\frac{\pi}{2}\ddot{y}\dot{y}, \tag{3.4}$$

$$P_V = C_{vortex}\dot{y}. \tag{3.5}$$

The kinetic energy ratio C_{EK} is introduced as the ratio of the cylinder's kinetic energy E_K to the fluid flow's kinetic energy, to quantify the cylinder's kinetic energy characteristics, as follows:

$$C_{EK} = \frac{0.5m_s\dot{Y}^2}{0.5m_f\dot{U_0}^2} = m^*\dot{y}^2. \tag{3.6}$$

When P_P and P_V are greater than zero, the fluid performs positive work on the cylinder and transfers energy into the system. Conversely, negative values indicate that the cylinder performs work on the fluid, resulting in energy transfer from the structure to the flow.

As shown in figure 13(*a–c*), the spectra of C_y and y for the cases of $L/D = 3.0$, $m^* = 0.2$; $L/D = 3.0$, $m^* = 6.5$; and $L/D = 5.5$, $m^* = 0.2$ are presented. Compared with figures 8 and 11, the dominant frequencies closely correspond to those of mode 2 identified in the DMD results. The dominant frequency component, $C_{y,m2}$, extracted from the transverse force coefficient, is used to evaluate the energy transfer associated with mode 2 between the EL cylinder and the fluid. Here, $C_{y,m2}$ is obtained through the fast Fourier transformation of C_y. Similar to (3.5), the corresponding power is calculated as $C_{y,m2}\dot{y}$, and the net energy transfer is evaluated by calculating its time-averaged value. For the

https://doi.org/10.1017/jfm.2026.11941 Published online by Cambridge University Press

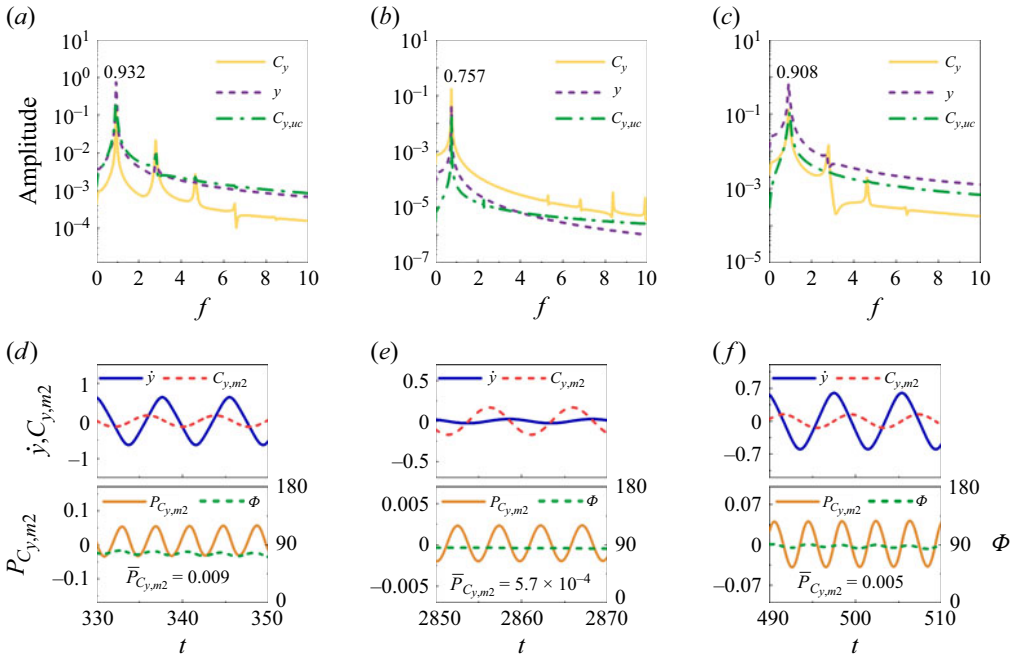


Figure 13. (*a–c*) Spectra of the displacement (y) of the EL cylinder and the transverse force coefficient (C_y) of the EL cylinder and the upstream cylinder; (*d–f*) time histories of velocity ($\dot{y}$), the dominant frequency component of the transverse force coefficient ($C_{y,m2}$), the power characteristic ($P_{C_{y,m2}}$) of $C_{y,m2}$ and the phase difference (Φ) between $\dot{y}$ and $C_{y,m2}$. (*a,d*) $L/D = 3.0$, $m^* = 0.2$; (*b,e*) $L/D = 3.0$, $m^* = 6.5$; and (*c,f*) $L/D = 5.5$, $m^* = 0.2$. The overbar denotes the cycle-averaged value, and $\bar{P}_{Cy,m2}$ is obtained by averaging over ten periods of $P_{C_{y,m2}}$.

case of $L/D = 3.0$ and $m^* = 0.2$ (figure 13*d*), mode 2 is the dominant mode governing the dynamic response of the system. In this case, the phase difference between $C_{y,m2}$ and the cylinder velocity $\dot{y}$ remains close to 90°, and the average power, $\bar{P}_{Cy,m2} = 0.009$, indicates effective energy transfer from the fluid flow to the EL cylinder. Consequently, the EL cylinder can sustain large-amplitude oscillations. When $L/D = 3.0$ and $m^* = 6.5$, mode 1 dominates the modal competition, and the system dynamics is therefore primarily governed by mode 1. Although the phase difference between $C_{y,m2}$ and $\dot{y}$ remains close to 90°, the average power is extremely small. As a result, the EL cylinder vibrates with an extremely small amplitude. At $L/D = 5.5$ and $m^* = 0.2$, the fully developed vortices in the gap flow cause mode 2 to become the primary mode governing the system dynamics. In this case, the average power, $\bar{P}_{Cy,m2} = 0.005$, indicates intense energy exchange between the cylinder and the fluid flow, and the EL cylinder exhibits significant vibration responses.

Under low-mass-ratio conditions, the added-mass effect has a significant influence on the EL-cylinder WIV system. The total transverse force acting on the cylinder can be decomposed into the potential-flow force and the vortex-shedding force. Here, we further analyse the energy-transfer characteristics associated with these two force components. Figure 14 presents the temporal evolution of energy transfer, surface pressure coefficients and instantaneous vorticity fields for representative cases in the LRV and IRV regimes, encompassing the AR, OS and CS flow regimes. Peaks in the Reynolds stress, indicated by black circles in the vorticity contours, identify vortex formation locations (Chopra & Mittal 2019; Sharma & Bhardwaj 2023). The out-of-phase relationship between P_P and P_V drives cyclic energy exchange, causing the cylinder to oscillate between its equilibrium

https://doi.org/10.1017/jfm.2026.11941 Published online by Cambridge University Press

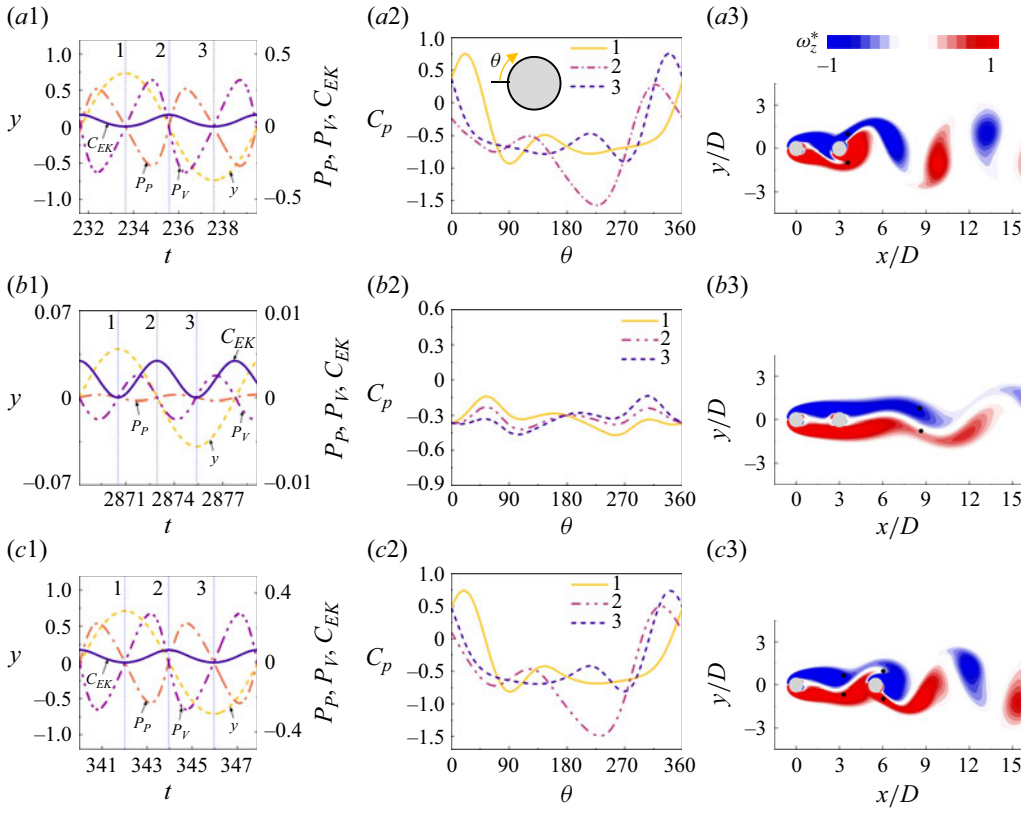


Figure 14. Time histories of displacement, the power of the potential and vortex-shedding forces, the kinetic energy coefficient, the instantaneous pressure coefficient on the EL-cylinder surface and the instantaneous vorticity fields of the EL-cylinder WIV at different L/D and m^*: (*a*) $L/D = 3.0$, $m^* = 0.2$; (*b*) $L/D = 3.0$, $m^* = 6.5$; and (*c*) $L/D = 5.5$, $m^* = 0.2$. Black circles in the vorticity contours indicate the locations of the maximum Reynolds stress, $\overline{\boldsymbol{u}'\boldsymbol{u}'}$.

and limit positions. From moment 1 to 2, the vortex-shedding force dominates the work input, driving the cylinder towards the equilibrium position (note that the system stiffness is zero, and thus no mechanical restoring force acts to return the cylinder to the centre position). During the interval from 2 to 3, the kinetic and potential forces propel the cylinder towards negative displacement. In the AR flow regime (figure 14*a*1–*a*3), vortex formation near the EL cylinder induces pronounced surface pressure fluctuations. Both the vortex-shedding force and the potential force provide substantial energy input to the EL-cylinder WIV system. The pressure-field DMD results (figure 9*b*.iv) reveal the second-order mode, antisymmetric about $y = 0$, with alternating high and low pressure that promote efficient fluid–structure energy exchange. Within the LRV regimes, as the flow mode transitions from the AR to the OS regime (figure 14*b*1–*b*3), a marked suppression of energy input is observed, as shown in figure 14(*b*1). Compared with the AR regime, both the work done by the potential force (P_P) and that by the vortex-shedding force (P_V) decrease significantly. In the OS regime, P_P is substantially smaller than P_V, rendering the vortex-shedding force dominant in the energy transfer. Since mode 2 loses its dominance in the modal competition with mode 1, the flow field around the EL cylinder becomes more stable compared with that in the AR flow regime. This stabilisation weakens surface-pressure fluctuations and suppresses fluid–structure energy

https://doi.org/10.1017/jfm.2026.11941 Published online by Cambridge University Press

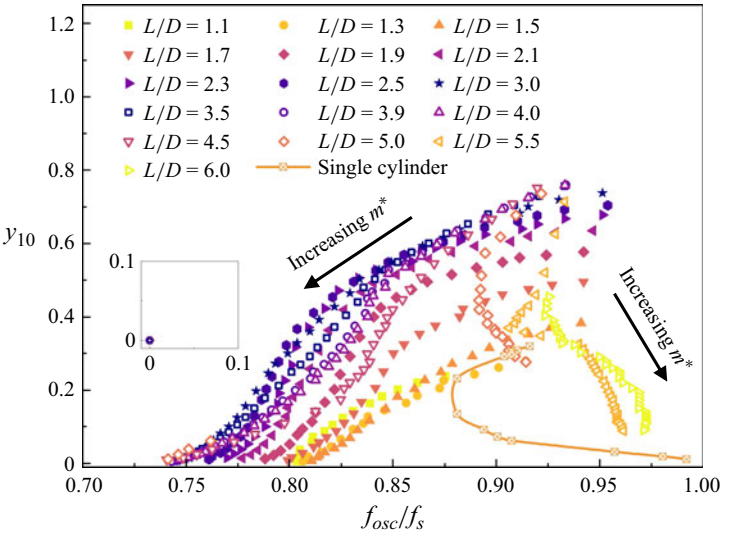


Figure 15. The dimensionless amplitude varies with frequency under different L/D and m^*.

exchange. In the IRV regime, the flow is characterised by the CS mode, in which fully developed vortices form within the gap region (with black circles denoting their formation locations). Unlike the single-cylinder case (see Appendix B), the presence of the downstream EL cylinder suppresses shear-layer separation from the upstream cylinder. Consequently, the vortex formation location relative to the upstream cylinder is reduced to $L_f/D \approx 3.3$, compared with $L_f/D = 3.9$ for a single cylinder. In the IRV regime, the EL cylinder experiences persistent vortex-shedding forces within the investigated m^* range. The DMD results (figure 12) reveal strong second- and fourth-order vorticity modes within the gap flow. In addition, high-gradient pressure-mode regions appear around the EL cylinder (figure 12*a*.iv), generating large pressure differences and enabling sustained energy exchange between the fluid and the EL cylinder.

4. Discussion

4.1. *Frequency response*

To examine the frequency response of the EL-cylinder WIV system, the vibration amplitudes in figure 5 are replotted against the corresponding frequencies, as shown in figure 15. The analysis focuses on the variation of vibration amplitude with the normalised frequency f_{osc}/f_s under different spacing ratios L/D and mass ratios m^*, with comparisons with the vibration responses of a single cylinder. The arrows indicate variations in mass ratio, where m^* increases from top to bottom. Navrose & Mittal (2017) investigated the frequency–amplitude response of a single cylinder under infinite U_r conditions at different Reynolds numbers. Below the critical mass ratio m^*_{cr}, the cylinder exhibited significant vibration amplitudes, which decreased with increasing m^*. Meanwhile, the frequency ratio initially decreased to a minimum and then increased as m^* increased, a trend consistent with the frequency–amplitude response shown in figure 15. However, under unsteady wake conditions, the frequency–amplitude response of the downstream EL cylinder exhibits pronounced variability. The vibration amplitude decreases monotonically with increasing m^*, consistent with the observation for a single cylinder that the minimum mass ratio corresponds to the maximum amplitude response.

https://doi.org/10.1017/jfm.2026.11941 Published online by Cambridge University Press

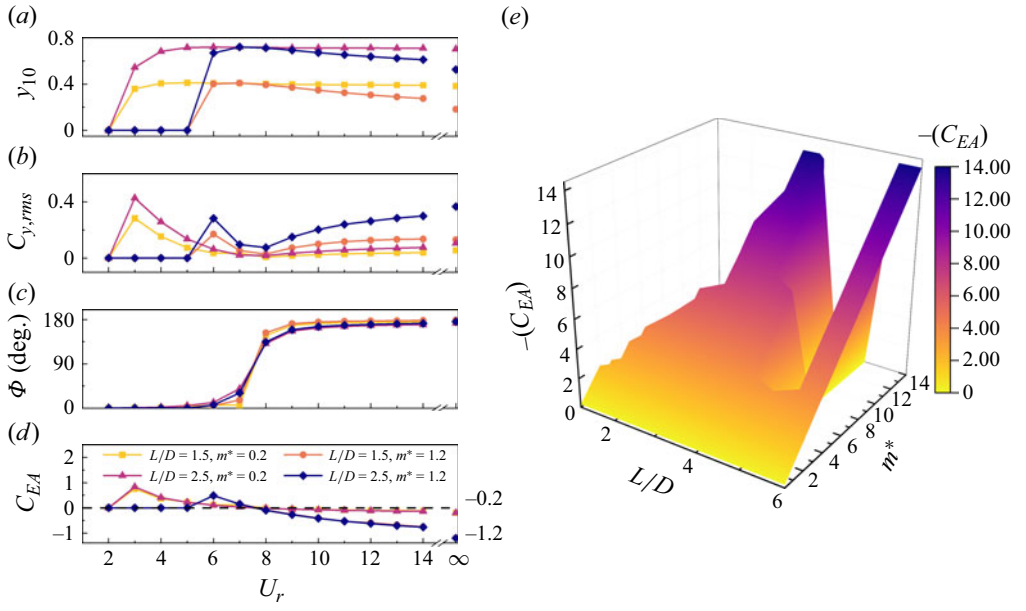


Figure 16. (*a*) The dimensionless amplitude y_{10}, (*b*) transverse force coefficient $C_{y,rms}$, (*c*) phase difference ϕ between the transverse force and displacement and (*d*) effective added-mass coefficient C_{EA} as functions of U_r for the EL-cylinder WIV system with a mechanical spring. (*e*) The variation of C_{EA} at infinite U_r in the parameter space of L/D and m^*.

For $L/D < 4.5$, the vibration frequency decreases with increasing m^*. At the minimum mass ratio $m^* = 0.2$, the vibration frequency gradually increases with increasing L/D. At the critical mass ratio m^*_{cr}, the amplitude y_{10} approaches zero, while the vibration frequency gradually decreases with L/D. When $L/D = 5$, the frequency trajectory exhibits distinct behaviour: at small m^*, the vibration frequency first decreases and then increases; as m^* increases to 2.6, the frequency drops sharply to $f_{osc}/f_s \approx 0.75$, accompanied by a significant reduction in vibration amplitude (see figure 5). Owing to the well-developed gap vortex, the gap flow at $L/D = 5$ is in a critical transitional state compared with cases with smaller spacing ratios. When $L/D = 5.5$, the flow mode undergoes a complete transition. The vibration frequency decreases from 0.92 to a minimum value of 0.89 and then gradually increases; however, its growth rate is lower than that observed for a single cylinder. A notable change in the amplitude growth trend occurs near $L/D = 3$, which correlates with vortex formation within the gap. As shown in figure 14(*c*3), the vortex formation length is $L_f/D = 3.3$. When the spacing ratio exceeds this value, the influence of the upstream shear layer on the EL-cylinder vibration amplitude is significantly weakened.

4.2. *Vibration response varies with reduced velocity*

Figure 16 illustrates the vibration responses as functions of the reduced velocity U_r, where ϕ denotes the phase difference between the transverse force and the displacement. The coefficient C_{EA} represents the effective added-mass coefficient, which characterises the apparent effect caused by the transverse force being in phase with the cylinder acceleration. Following the formulation established by Govardhan & Williamson (2002),

https://doi.org/10.1017/jfm.2026.11941 Published online by Cambridge University Press

$$C_{EA} = \frac{C_y cos(\phi)}{2\pi^3 A_y St^2}\left(\frac{f_{v0}}{f_{osc}}\right)^2 = \frac{C_y cos(\phi)}{2\pi^3 A_y}\left(\frac{U}{f_{osc} D}\right)^2. \tag{4.1}$$

Govardhan & Williamson (2002) analysed the behaviour of C_{EA} for a single cylinder under infinite U_r conditions (i.e. in the absence of mechanical springs) in VIV experiments. They reported that as U_r approaches infinity, C_{EA} gradually tends to $-m^*$ when m^* is below the critical mass ratio.

As the reduced velocity U_r increases, a larger vibration amplitude is observed at $L/D = 2.5$, owing to enhanced shear-layer interaction with the EL cylinder. In previous work, Borazjani & Sotiropoulos (2009) performed EL-cylinder WIV simulations at $Re = 200$ and $L/D = 1.5$, showing that the vibration amplitude gradually decreased with increasing U_r. The lift coefficient C_y acting on the cylinder first decreased to a minimum and then increased as U_r increased. These findings are consistent with the present results. In contrast, experiments reported divergent vibrations at higher reduced velocity, which were attributed to differences in Reynolds number (Assi *et al.* 2010). Notably, C_{EA} approaches zero near $U_r = 7$–8, where the vibration amplitude becomes independent of m^*, and the phase difference undergoes an out-of-phase transition. A similar phenomenon was reported by Navrose & Mittal (2017) for the VIV of a single cylinder. Under $U_r = \infty$ in the EL-cylinder WIV system, C_{EA} tends to $-m^*$, consistent with the behaviour of a single cylinder. Within the parameter domain m^*, L/D, it is likewise satisfied that when $U_r \to \infty$, if cylinder vibration persists, then $C_{EA} = -m^*$, as shown in figure 16(*e*). It can be observed that in the LRV and IRV regimes, the effective added-mass coefficient varies linearly with the mass ratio.

4.3. *Wake stiffness concept at low Reynolds numbers*

The WIV experiments of Assi *et al.* (2013) show that, at high Reynolds numbers, the oscillation amplitude of the downstream cylinder increases continuously with increasing Reynolds number *Re*. Assi *et al.* (2013) introduced the concept of 'wake stiffness' based on the static lift gradient at different transverse locations and pointed out that the vibration frequency of the downstream cylinder does not coincide with the vortex-shedding frequency of the stationary upstream cylinder, but is instead governed by the 'wake stiffness' effect. At low Reynolds numbers, the amplitude and frequency responses of the EL cylinder differ from those observed at high Reynolds numbers. The phase-difference results in figure 16(*c*) show that the phase difference between the transverse force coefficient and the displacement of the downstream cylinder is 180°, suggesting that, in the absence of mechanical stiffness, the fluid force induced by the upstream wake also acts as an effective restoring force. However, this mechanism differs fundamentally from WIV at high Reynolds numbers. At $Re = 60$, when m^* exceeds the critical mass ratio, m^*_{cr}, the entire flow field becomes stable, and vortex shedding is suppressed, thereby preventing effective wake excitation. Under the OS flow regime, the vibration of the EL cylinder is primarily governed by the vortex shedding generated behind itself, and the applicability of the 'wake stiffness' concept becomes limited. In contrast, under the AR flow regime, the shear layers separated from the upstream cylinder alternately attach to the surface of the EL cylinder, resulting in larger-amplitude responses. The spectral results in figure 13(*a–c*) show that the dominant frequencies of the transverse forces acting on both the upstream cylinder and the EL cylinder, as well as the displacement of the EL cylinder, are identical. This indicates that the vibration response of the EL cylinder is related to the periodic excitation induced by the upstream wake flow. The study of Mysa *et al.* (2016) also demonstrated that the vibration mechanism of the downstream cylinder is

https://doi.org/10.1017/jfm.2026.11941 Published online by Cambridge University Press

primarily governed by the interaction between the cylinder motion and the vortex shedding from the upstream cylinder. These observations suggest that, at low Reynolds numbers, the applicability of the wake stiffness concept is weakened.

5. Conclusions

In this study, the FIVs of an EL cylinder in the wake of a fixed upstream cylinder are numerically investigated. The focus is placed on the existence and characteristics of a critical mass ratio under unsteady wake conditions at $U_r \to \infty$.

Vibration responses across the L/D and m^* parameter domains reveal three distinct regimes: LRV regime, IRV regime and NV regime. Simulation results confirm that a critical mass ratio m^*_{cr} exists at the LRV–NV transition boundary, even for cylinders subjected to unsteady wake. Notably, the amplitude diminishes to zero at m^*_{cr}, contrasting with the abrupt amplitude increase observed in single cylinders below m^*_{cr}.

Flow-field analyses reveal that m^*_{cr} correlates with flow regime transitions. In the LRV regime, increasing m^* induces flow transitions from the AR regime or COWAR regime to steady flow. The Kármán vortex street (mode 2) exhibits significant modal energy contributions in the AR/COWAR mode. As m^* approaches m^*_{cr}, mode 2 energy contributions gradually reduce to zero, coinciding with amplitude extinction. In the IRV regime, the flow exhibits CS modes, where mode 2 maintains substantial energy contributions, and no critical mass ratio is observed within the m^* range. The value of m^*_{cr} is governed by L/D and the vortex formation length L_f/D of a stationary single cylinder. When $L/D < L_f/D$, m^*_{cr} increases with L/D; conversely, when $L/D > L_f/D$, m^*_{cr} decreases as L/D increases.

The present study is restricted to a two-dimensional tandem-cylinder configuration at $Re = 60$, with transverse vibration only and without structural damping. Future work should examine the robustness of the present stability boundary under more realistic conditions, including three-dimensional effects, finite structural damping and higher Reynolds numbers.

Funding. This work was supported by the National Natural Science Foundation of China (grant nos. 12302317, 52277227, 12425206), the Rolling Support Program for Excellent Young Scientists Fund of Henan Province (grant no. 252300421239), the XJTU Young Talent Support Plan and the Fundamental Research Funds for the Central Universities (grant no. xtr052025027).

Declaration of interests. The authors report no conflict of interest.

Data availability statement. The data that support the findings of this study are available from the corresponding author upon reasonable request.

Appendix A. Numerical convergence analysis

A numerical convergence study was conducted for the tandem-cylinder configuration at $L/D = 3$ and $m^* = 1.0$ to determine the appropriate mesh resolution and time-step size for the simulations. In the mesh-independence verification, a mesh refinement factor of $r = 2$ was adopted, meaning that the grid spacing of each refined size is half that of the previous one (Eça & Hoekstra 2014). Considering the relatively small gap spacing in the present studies, the resolution of the first mesh size was set to $\Delta g = 1/50D$, where D is the cylinder diameter. Simultaneously, the time step Δt was set to 0.006, 0.003 and 0.0015. The specific settings are summarised in table 2. Four physical quantities were monitored: vibration amplitude, transverse force coefficient, drag coefficient and Strouhal number. For cases 1#, 2# and 3#, the grid convergence index for case 1#, calculated based on the

https://doi.org/10.1017/jfm.2026.11941 Published online by Cambridge University Press

Case	Δg	Δt	Nodes	y_{max}	$C_{y,rms}$	$C_{D,mean}$	St
1#	1/50	0.003	1 436 349	0.5714	0.3459	0.7233	0.1175
2#	1/100	0.003	4 919 296	0.5728	0.3468	0.7281	0.1175
3#	1/200	0.003	1 6 392 192	0.5733	0.3471	0.7286	0.1170
4#	1/50	0.006	1 436 349	0.5721	0.3462	0.7221	0.1175
5#	1/50	0.0015	1 436 349	0.5713	0.3457	0.7233	0.1175

Table 2. Results of the EL-cylinder WIV system for varying grid resolutions and time steps.

Case	L_u	L_d	Nodes	y_{max}	$C_{y,rms}$	$C_{D,mean}$	St
1#	10	15	1 436 349	0.5714	0.3459	0.7233	0.1175
2#	15	20	1 933 459	0.5710	0.3446	0.7215	0.1175
3#	20	30	2 806 449	0.5707	0.3450	0.7159	0.1175

Table 3. Results of the EL-cylinder WIV system for different domain sizes.

maximum cylinder displacement y_{max}, was 0.17 %, indicating that the mesh configuration is well converged. Furthermore, the relative errors of other physical quantities (with case 3# as the reference) were less than 0.73 %, confirming that a mesh resolution of $1/50D$ is sufficient for the present simulations. Time-step sensitivity was assessed using cases 1#, 4# and 5#. The maximum difference for case 1# (relative to case 5#) was 0.06 %, satisfying the temporal convergence requirement. Based on these results, the grid resolution and time step of case 1# were selected for the subsequent simulations, corresponding to 2049 uniformly distributed grid points in the x direction.

The influence of computational domain size was further examined. Three computational domain configurations were tested, with the domain width varying from $30D$ to $60D$, and the distance between the upstream cylinder and the inlet varying from $10D$ to $20D$, as shown in table 3. The mesh resolution and time step were kept fixed at $\Delta g = 1/50D$ and $\Delta t = 0.003$, respectively. The corresponding results are also presented in table 3. Based on case 3#, the variations in cylinder vibration amplitude, transverse force coefficient, drag coefficient and Strouhal number were all below 1.0 %. Therefore, the computational domain parameters were selected as $L_u = 10D$ and $L_d = 15D$ for the present study.

Appendix B. Flow around a fixed cylinder at $Re = 60$

Using the same grid resolution and time-step size as those adopted for the EL-cylinder WIV system, the flow around a fixed single cylinder at a Reynolds number of 60 is simulated. The analysis focuses on the vortex formation length (L_f), defined as the distance from the centre of the cylinder to the location where vortices develop and are shed. Chopra & Mittal (2019) reviewed various methods for determining L_f. In the present study, the criterion based on the Reynolds stress component $\overline{\boldsymbol{u}'\boldsymbol{u}'}$ is employed. The vortex formation length L_f is calculated as the distance between the location of maximum Reynolds stress and the centre of the cylinder. Here, $\boldsymbol{u}'$ denotes the fluctuation of the streamwise velocity component relative to the time-averaged flow. Figure 17 presents the vorticity field and the corresponding vortex formation length for a single cylinder. It is observed that $L_f/D = 3.9$, which is larger than the value shown in figure 14, owing to the

https://doi.org/10.1017/jfm.2026.11941 Published online by Cambridge University Press

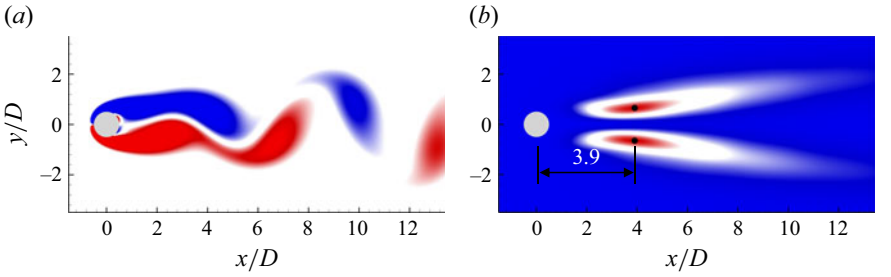


Figure 17. (*a*) Vorticity field and (*b*) corresponding vortex formation length L_f for flow past a fixed cylinder at $Re = 60$.

absence of obstruction effects from the downstream EL cylinder on the shear layer of the fixed cylinder.

References

ALAM, M.M. 2016 Lift forces induced by phase lag between the vortex sheddings from two tandem bluff bodies. *J. Fluids Struct.* **65**, 217–237.

ALAM, M.M., CHEN, G., ZHOU, Y., WANG, L., WANG, J. & ISLAM, M.D. 2023 Flow-induced vibration of a cantilevered cylinder in the wake of another. *J. Fluids Struct.* **120**, 103901.

ALAM, M.M., LIU, J., ZHOU, Y., ZHU, H. & JI, C. 2025 Wake-induced vibration of an inelastic cylinder. *J. Fluid Mech.* **1015**, A46.

ALAM, M.M., MORIYA, M., TAKAI, K. & SAKAMOTO, H. 2003 Fluctuating fluid forces acting on two circular cylinders in a tandem arrangement at a subcritical Reynolds number. *J. Wind Engng Ind. Aerodyn.* **91** (1), 139–154.

ASSI, G.R.S., BEARMAN, P.W., CARMO, B.S., MENEGHINI, J.R., SHERWIN, S.J. & WILLDEN, R.H.J. 2013 The role of wake stiffness on the wake-induced vibration of the downstream cylinder of a tandem pair. *J. Fluid Mech.* **718**, 210–245.

ASSI, G., BEARMAN, P. & MENEGHINI, J. 2010 On the wake-induced vibration of tandem circular cylinders: the vortex interaction excitation mechanism. *J. Fluid Mech.* **661**, 365–401.

BAGHERI, S. 2013 Koopman-mode decomposition of the cylinder wake. *J. Fluid Mech.* **726**, 596–623.

BAO, Y., HUANG, C., ZHOU, D., TU, J. & HAN, Z. 2012 Two-degree-of-freedom flow-induced vibrations on isolated and tandem cylinders with varying natural frequency ratios. *J. Fluids Struct.* **35**, 50–75.

BARRERO-GIL, A., SANZ-ANDRÉS, A. & ALONSO, G. 2009 Hysteresis in transverse galloping: the role of the inflection points. *J. Fluids Struct.* **25** (6), 1007–1020.

BELANGER, F., PAIDOUSSIS, M.P. & DE LANGRE, E. 1995 Time-marching analysis of fluid-coupled systems with large added mass. *AIAA J.* **33** (4), 752–757.

BOKAIAN, A. & GEOOLA, F. 1984 Wake-induced galloping of two interfering circular cylinders. *J. Fluid Mech.* **146**, 383–415.

BORAZJANI, I. & SOTIROPOULOS, F. 2009 Vortex-induced vibrations of two cylinders in tandem arrangement in the proximity–wake interference region. *J. Fluid Mech.* **621**, 321–364.

BOURGUET, R. 2023 Path curvature enhances the flow-induced vibrations of a cylinder without structural restoring force. *J. Fluid Mech.* **977**, A31.

BOURGUET, R. 2024 Flow-induced vibrations with and without structural restoring force: convergence under the effect of path curvature. *J. Fluid Mech.* **984**, A51.

CARBERRY, J., SHERIDAN, J. & ROCKWELL, D. 2001 Forces and wake modes of an oscillating cylinder. *J. Fluids Struct.* **15** (3), 523–532.

CARMO, B.S., SHERWIN, S.J., BEARMAN, P.W. & WILLDEN, R.H.J. 2011 Flow-induced vibration of a circular cylinder subjected to wake interference at low Reynolds number. *J. Fluids Struct.* **27** (4), 503–522.

CHOPRA, G. & MITTAL, S. 2019 Drag coefficient and formation length at the onset of vortex shedding. *Phys. Fluids* **31** (1), 013601.

EÇA, L. & HOEKSTRA, M. 2014 A procedure for the estimation of the numerical uncertainty of CFD calculations based on grid refinement studies. *J. Comput. Phys.* **262**, 104–130.

FAN, X., WANG, Y. & TAN, W. 2021 Aerodynamic wake oscillator for modeling flow-induced vibration of tandem cylinders with short spans. *Intl J. Mech. Sci.* **204**, 106548.

https://doi.org/10.1017/jfm.2026.11941 Published online by Cambridge University Press

GABBAI, R.D. & BENAROYA, H. 2005 An overview of modeling and experiments of vortex-induced vibration of circular cylinders. *J. Sound Vib.* **282** (3), 575–616.

GERRARD, J.H. 1966 The mechanics of the formation region of vortices behind bluff bodies. *J. Fluid Mech.* **25** (2), 401–413.

GOVARDHAN, R. & WILLIAMSON, C.H.K. 2002 Resonance forever: existence of a critical mass and an infinite regime of resonance in vortex-induced vibration. *J. Fluid Mech.* **473**, 147–166.

GRIFFIN, O.M. & RAMBERG, S.E. 1974 The vortex-street wakes of vibrating cylinders. *J. Fluid Mech.* **66** (3), 553–576.

HAN, P. & DE LANGRE, E. 2021 There is no critical mass ratio for galloping of a square cylinder under flow. *J. Fluid Mech.* **931**, A27.

HAN, P., DE LANGRE, E., THOMPSON, M.C., HOURIGAN, K. & ZHAO, J. 2023*b* Vortex-induced vibration forever even with high structural damping. *J. Fluid Mech.* **962**, A13.

HAN, P., HUANG, W.-X., QIN, D., WANG, J. & ZHAO, J. 2023*a* An analytical model for estimating the maximum energy harvesting efficiency from vortex-induced vibration. *J. Fluids Struct.* **122**, 103961.

HAN, P., ZHANG, J.-D., ZHANG, D. & HUANG, W.-X. 2025 How a self-propelled fin gains hydrodynamic advantages behind a circular cylinder with vortex-induced vibrations. *J. Fluid Mech.* **1011**, A26.

HAN, P., ZHOU, C., SHI, Y., FENG, K., WANG, J. & ZHAO, J. 2026 Vortex-induced vibration forever of an ultra-light circular cylinder for robust energy harvesting from fluid flow. *Ocean Engng* **352**, 124296.

HU, Z., WANG, J. & SUN, Y. 2020 Flow-induced vibration of one-fixed-one-free tandem arrangement cylinders with different mass-damping ratios using wind tunnel experiment. *J. Fluids Struct.* **96**, 103019.

HUANG, W.-X., SHIN, S.J. & SUNG, H.J. 2007 Simulation of flexible filaments in a uniform flow by the immersed boundary method. *J. Comput. Phys.* **226** (2), 2206–2228.

HUANG, W.-X. & SUNG, H.J. 2010 Three-dimensional simulation of a flapping flag in a uniform flow. *J. Fluid Mech.* **653**, 301–336.

HUANG, W.-X. & SUNG, H.J. 2009 An immersed boundary method for fluid–flexible structure interaction. *Comput. Meth. Appl. Mech. Engng* **198** (33), 2650–2661.

HUERA-HUARTE, F. 2025 Vortex-induced vibration of flexible cylinders in cross-flow. *Annu. Rev. Fluid Mech.* **57**, 285–310.

KIM, K., BAEK, S.-J. & SUNG, H.J. 2002 An implicit velocity decoupling procedure for the incompressible navier–stokes equations. *Intl J. Numer. Meth. Flow* **38** (2), 125–138.

KODA, Y. & LIEN, F.-S. 2013 Aerodynamic effects of the early three-dimensional instabilities in the flow over one and two circular cylinders in tandem predicted by the lattice Boltzmann method. *Comput. Fluids* **74**, 32–43.

KONSTANTINIDIS, E., DOROGI, D. & BARANYI, L. 2021 Resonance in vortex-induced in-line vibration at low Reynolds numbers. *J. Fluid Mech.* **907**, A34.

LI, X., ZHANG, W. & GAO, C. 2018 Proximity-interference wake-induced vibration at subcritical *Re*: mechanism analysis using a linear dynamic model. *Phys. Fluids* **30** (3), 033606.

LIN, K., SUN, Y., LIU, H., ZHU, Y., WANG, J., TRIANTAFYLLOU, M.S. & FAN, D. 2024 Mapping the properties of wake-induced vibration on a circular cylinder. *J. Fluid Mech.* **1001**, A33.

LIN, K., WANG, J., ZHENG, H. & SUN, Y. 2020 Numerical investigation of flow-induced vibrations of two cylinders in tandem arrangement with full wake interference. *Phys. Fluids* **32** (1), 015112.

LO, J.C.C., THOMPSON, M.C., HOURIGAN, K. & ZHAO, J. 2024 Order of magnitude increase in power from flow-induced vibrations. *Renew. Sustain. Energy Rev.* **205**, 114843.

LUO, F., GAO, C. & ZHANG, W. 2022 The key to suppress vortex-induced vibration: stability of the structural mode. *J. Fluids Struct.* **113**, 103692.

MAHÍR, N. & ALTAÇ, Z. 2008 Numerical investigation of convective heat transfer in unsteady flow past two cylinders in tandem arrangements. *Intl J. Heat Fluid Flow* **29** (5), 1309–1318.

MENEGHINI, J.R., SALTARA, F., SIQUEIRA, C.L.R. & FERRARI, J.A. 2001 Numerical simulation of flow interference between two circular cylinders in tandem and side-by-side arrangements. *J. Fluids Struct.* **15** (2), 327–350.

MENON, K. & MITTAL, R. 2020 Dynamic mode decomposition based analysis of flow over a sinusoidally pitching airfoil. *J. Fluids Struct.* **94**, 102886.

MISHRA, R., SOTI, A., BHARDWAJ, R., KULKARNI, S.S. & THOMPSON, M.C. 2020 Transverse vortex-induced vibration of a circular cylinder on a viscoelastic support at low Reynolds number. *J. Fluids Struct.* **95**, 102997.

MORSE, T.L. & WILLIAMSON, C.H.K. 2009 Prediction of vortex-induced vibration response by employing controlled motion. *J. Fluid Mech.* **634**, 5–39.

MYSA, R.C., KABOUDIAN, A. & JAIMAN, R.K. 2016 On the origin of wake-induced vibration in two tandem circular cylinders at low Reynolds number. *J. Fluids Struct.* **61**, 76–98.

https://doi.org/10.1017/jfm.2026.11941 Published online by Cambridge University Press

NAVROSE, MITTAL, S. 2017 The critical mass phenomenon in vortex-induced vibration at low Re. *J. Fluid Mech.* **820**, 159–186.

NGUYEN, V., CHAN, W. & NGUYEN, H.-H. 2018 Numerical investigation of wake induced vibrations of cylinders in tandem arrangement at subcritical Reynolds numbers. *Ocean Engng* **154**, 341–356.

SHARMA, G. & BHARDWAJ, R. 2023 Flow-induced vibrations of elastically coupled tandem cylinders. *J. Fluid Mech.* **976**, A22.

SHIELS, D., LEONARD, A. & ROSHKO, A. 2001 Flow-induced vibration of a circular cylinder at limiting structural parameters. *J. Fluids Struct.* **15** (1), 3–21.

SUMNER, D. 2010 Two circular cylinders in cross-flow: a review. *J. Fluids Struct.* **26** (6), 849–899.

UDDIN, E., HUANG, W.-X. & SUNG, H.J. 2015 Actively flapping tandem flexible flags in a viscous flow. *J. Fluid Mech.* **780**, 120–142.

WANG, L.J., ALAM, M.M. & ZHOU, Y. 2018 Two tandem cylinders of different diameters in cross-flow: effect of an upstream cylinder on wake dynamics. *J. Fluid Mech.* **836**, 5–42.

WANG, J., FAN, D. & LIN, K. 2020*a* A review on flow-induced vibration of offshore circular cylinders. *J. Hydrodyn.* **32** (3), 415–440.

WANG, W., SONG, B., MAO, Z., TIAN, W., ZHANG, T. & HAN, P. 2020*b* Numerical investigation on vortex-induced vibration of bluff bodies with different rear edges. *Ocean Engng* **197**, 106871.

WILLIAMSON, C.H.K. & GOVARDHAN, R. 2004 Vortex-induced vibrations. *Annu. Rev. Fluid Mech.* **36** (1), 413–455.

WILLIAMSON, C.H.K. & GOVARDHAN, R. 2008 A brief review of recent results in vortex-induced vibrations. *J. Wind Engng Ind. Aerodyn.* **96** (6–7), 713–735.

XU, L., LIU, Z., LI, X., ZHAO, M. & ZHAO, Y. 2023 An improved mode time coefficient for dynamic mode decomposition. *Phys. Fluids* **35** (10), 105106.

YU, Z., PING, H., WANG, E., BAO, Y., XU, H., HUANG, Y. & XIAO, Q. 2025 Missing critical mass ratio in VIV of rigidly connected cylinders. *Intl J. Mech. Sci.* **295**, 110236.

YVIN, C., LEROYER, A., VISONNEAU, M. & QUEUTEY, P. 2018 Added mass evaluation with a finite-volume solver for applications in fluid–structure interaction problems solved with co-simulation. *J. Fluids Struct.* **81**, 528–546.

ZDRAVKOVICH, M.M. 1987 The effects of interference between circular cylinders in cross flow. *J. Fluids Struct.* **1** (2), 239–261.

ZHANG, M., SONG, Y., ABDELKEFI, A., YU, H. & WANG, J. 2022 Vortex-induced vibration of a circular cylinder with nonlinear stiffness: prediction using forced vibration data. *Nonlinear Dyn.* **108** (3), 1867–1884.

ZHAO, M. 2013 Flow induced vibration of two rigidly coupled circular cylinders in tandem and side-by-side arrangements at a low Reynolds number of 150. *Phys. Fluids* **25** (12), 123601.

ZHAO, M. 2023 A review of recent studies on the control of vortex-induced vibration of circular cylinders. *Ocean Engng* **285** (2), 115389.

ZHU, H., ZHANG, C. & LIU, W. 2019 Wake-induced vibration of a circular cylinder at a low Reynolds number of 100. *Phys. Fluids* **31** (7), 073606.

ZHU, H., ZHONG, J. & ZHOU, T. 2021 Wake structure characteristics of three tandem circular cylinders at a low Reynolds number of 160. *Phys. Fluids* **33** (4), 044113.

https://doi.org/10.1017/jfm.2026.11941 Published online by Cambridge University Press